


# VLT-MATISSE chromatic aperture-synthesis imaging of $\eta$ Carinae's stellar wind across the Br $\alpha$ line

## Periastron passage observations in February 2020<sup>★</sup>

G. Weigelt<sup>1</sup> , K.-H. Hofmann<sup>1</sup>, D. Schertl<sup>1</sup>, B. Lopez<sup>2</sup>, R. G. Petrov<sup>2</sup>, S. Lagarde<sup>2</sup>, Ph. Berio<sup>2</sup>, W. Jaffe<sup>3</sup>, Th. Henning<sup>4</sup>, F. Millour<sup>2</sup>, A. Meilland<sup>2</sup>, F. Allouche<sup>2</sup>, S. Robbe-Dubois<sup>2</sup>, A. Matter<sup>2</sup>, P. Cruzalèbes<sup>2</sup>, D. J. Hillier<sup>5</sup>, C. M. P. Russell<sup>6</sup>, T. Madura<sup>7</sup>, T. R. Gull<sup>8</sup>, M. F. Corcoran<sup>6,9</sup>, A. Daminieli<sup>10</sup>, A. F. J. Moffat<sup>11</sup>, P. W. Morris<sup>12</sup>, N. D. Richardson<sup>13</sup>, C. Paladini<sup>14</sup>, M. Schöller<sup>15</sup>, A. Mérand<sup>15</sup>, A. Glindemann<sup>15</sup>, U. Beckmann<sup>1</sup>, M. Heininger<sup>1</sup>, F. Bettonvil<sup>3</sup>, G. Zins<sup>14</sup>, J. Woillez<sup>15</sup>, P. Bristow<sup>15</sup>, J. Sanchez-Bermudez<sup>4,16</sup>, K. Ohnaka<sup>17</sup>, S. Kraus<sup>18</sup>, A. Mehner<sup>14</sup>, M. Wittkowski<sup>15</sup>, C. A. Hummel<sup>15</sup>, P. Stee<sup>2</sup>, F. Vakili<sup>2</sup>, H. Hartman<sup>19</sup>, F. Navarete<sup>10</sup>, K. Hamaguchi<sup>9,20</sup>, D. A. Espinoza-Galeas<sup>9</sup>, I. R. Stevens<sup>21</sup>, R. van Boekel<sup>4</sup>, S. Wolf<sup>22</sup>, M. R. Hogerheijde<sup>3,23</sup>, C. Dominik<sup>23</sup>, J.-C. Augereau<sup>24</sup>, E. Pantin<sup>25</sup>, L. B. F. M. Waters<sup>26,27</sup>, K. Meisenheimer<sup>4</sup>, J. Varga<sup>3,30</sup>, L. Klarmann<sup>4</sup>, V. Gámez Rosas<sup>3</sup>, L. Burtscher<sup>3</sup>, J. Leftley<sup>2</sup>, J. W. Isbell<sup>4</sup>, V. Hócdé<sup>2</sup>, G. Yoffe<sup>4</sup>, E. Kokoulina<sup>2</sup>, J. Hron<sup>28</sup>, J. Groh<sup>29</sup>, A. Kreplin<sup>18</sup>, Th. Rivinius<sup>14</sup>, W.-J. de Wit<sup>14</sup>, W.-C. Danchi<sup>2,8</sup>, A. Domiciano de Souza<sup>2</sup>, J. Drevon<sup>2</sup>, L. Labadie<sup>31</sup>, C. Connot<sup>1</sup>, E. Nußbaum<sup>1</sup>, M. Lehmitz<sup>4</sup>, P. Antonelli<sup>2</sup>, U. Graser<sup>4</sup>, and C. Leinert<sup>4</sup>

(Affiliations can be found after the references)

Received 3 May 2021 / Accepted 30 June 2021

### ABSTRACT

**Context.** Eta Carinae is a highly eccentric, massive binary system (semimajor axis  $\sim 15.5$  au) with powerful stellar winds and a phase-dependent wind-wind collision (WWC) zone. The primary star,  $\eta$  Car A, is a luminous blue variable (LBV); the secondary,  $\eta$  Car B, is a Wolf-Rayet or O star with a faster but less dense wind. Aperture-synthesis imaging allows us to study the mass loss from the enigmatic LBV  $\eta$  Car. Understanding LBVs is a crucial step toward improving our knowledge about massive stars and their evolution.

**Aims.** Our aim is to study the intensity distribution and kinematics of  $\eta$  Car's WWC zone.

**Methods.** Using the VLT-MATISSE mid-infrared interferometry instrument, we perform Br $\alpha$  imaging of  $\eta$  Car's distorted wind.

**Results.** We present the first VLT-MATISSE aperture-synthesis images of  $\eta$  Car A's stellar wind in several spectral channels distributed across the Br $\alpha$  4.052  $\mu\text{m}$  line (spectral resolving power  $R \sim 960$ ). Our observations were performed close to periastron passage in February 2020 (orbital phase  $\sim 14.0022$ ). The reconstructed iso-velocity images show the dependence of the primary stellar wind on wavelength or line-of-sight (LOS) velocity with a spatial resolution of 6 mas ( $\sim 14$  au). The radius of the faintest outer wind regions is  $\sim 26$  mas ( $\sim 60$  au). At several negative LOS velocities, the primary stellar wind is less extended to the northwest than in other directions. This asymmetry is most likely caused by the WWC. Therefore, we see both the velocity field of the undisturbed primary wind and the WWC cavity. In continuum spectral channels, the primary star wind is more compact than in line channels. A fit of the observed continuum visibilities with the visibilities of a stellar wind CMFGEN model (CMFGEN is an atmosphere code developed to model the spectra of a variety of objects) provides a full width at half maximum fit diameter of the primary stellar wind of  $2.84 \pm 0.06$  mas ( $6.54 \pm 0.14$  au). We compare the derived intensity distributions with the CMFGEN stellar wind model and hydrodynamic WWC models.

**Key words.** stars: winds, outflows – stars: individual:  $\eta$  Carinae – stars: massive – stars: mass-loss – binaries: general – techniques: interferometric

## 1. Introduction

Eta Car is a spectacular, unstable binary system at a distance of  $\sim 2.3$  kpc (Davidson & Humphreys 1997; Smith 2006). The primary star,  $\eta$  Car A, is a very massive ( $M \sim 100 M_{\odot}$ ) luminous blue variable star (LBV) with an optically thick stellar wind, a mass-loss rate of  $\sim 10^{-3} M_{\odot} \text{ yr}^{-1}$ , and a terminal wind speed of  $\sim 420 \text{ km s}^{-1}$  (Davidson & Humphreys 1997, 2012; Davidson et al. 2001; Hillier et al. 2001, 2006; Smith 2006; Groh et al.

2012b); the secondary star,  $\eta$  Car B, is probably a hot Of or Wolf-Rayet (WR) star. Its wind is believed to be characterized by a mass-loss rate of  $\sim 10^{-5} M_{\odot} \text{ yr}^{-1}$  and a terminal wind speed of  $\sim 3000 \text{ km s}^{-1}$  (Pittard & Corcoran 2002; Corcoran 2005; Verner et al. 2005; Gull et al. 2009; Mehner et al. 2010; Madura et al. 2012). Daminieli discovered that  $\eta$  Car is an eccentric ( $e \sim 0.9$ ) binary with a period of 5.54 yr and a semimajor axis of  $\sim 15.5$  au (Daminieli 1996; Daminieli et al. 1997, 1998).

Eta Car's X-ray variability is caused by the collision of the stellar wind of the primary star with the stellar wind of the secondary star (Corcoran et al. 1997; Ishibashi et al. 1999; Pittard & Corcoran 2002; Corcoran 2005). The orbital eccentricity causes a phase-dependent wind-wind collision (WWC) zone

<sup>★</sup> Based on observations collected at the European Organisation for Astronomical Research in the Southern Hemisphere under ESO program 0104.D-0015A, 0104.D-0015B, 0104.D-0015C, 0106.D-0309(A), 0106.D-0309(B), and 0106.D-0309(C).

in the form of a shock cone or cavity, whose shape is modified by the relative orbits of the stars. The WWC and the binary system were studied using many different methods (Damineli et al. 1997; Davidson 1997; Corcoran et al. 1997, 2001, 2017; Pittard & Corcoran 2002; Corcoran 2005; Nielsen et al. 2007; Soker 2007; Humphreys et al. 2008; Gull et al. 2009, 2011; Groh et al. 2010b, 2012a,b; Mehner et al. 2010, 2012, 2011; Smith 2010; Richardson et al. 2016; Weigelt et al. 2016; Gravity Collaboration 2018; Millour et al. 2020).

Observations by the *Hubble* Space Telescope allow high spatial and high spectral resolution imaging of the circumstellar environment of  $\eta$  Car at many orbital phases (Gull et al. 2009, 2011, 2016; Mehner et al. 2010, 2011, 2012; Teodoro et al. 2013). The resolved circumbinary WWC structures, which were resolved in many emission lines, are called fossil wind structures. They are the result of the WWC process and the accumulation of material over several orbital cycles. To improve the theoretical understanding of the wind collision, various 3D hydrodynamic models of the wind collision have been developed (e.g., Okazaki et al. 2008; Parkin et al. 2011; Madura et al. 2012, 2013; Clementel et al. 2015; Kashi 2019; Russell et al. 2016).

Infrared interferometric observations of  $\eta$  Car with a spatial resolution of a few mas provide us with a unique opportunity to improve our understanding of the optically thick stellar wind of the primary star and the WWC zone. Interferometric visibility measurements are able to resolve  $\eta$  Car's wind region in the  $K$ -band continuum (van Boekel et al. 2003; Kervella 2007; Weigelt et al. 2007). Visibility and closure phase studies in the continuum and in emission lines are reported by Weigelt et al. (2007, 2016) and Gravity Collaboration (2018). The derived diameters of  $\eta$  Car A's stellar wind agree with predictions from CMFGEN stellar wind models. CMFGEN is an atmosphere code developed to model the spectra of a variety of objects (Hillier & Miller 1998; Hillier et al. 2001, 2006). The  $K$ -band continuum uniform disk radius of the intensity distribution of  $\eta$  Car's optically thick primary stellar wind is  $\sim 1$  mas ( $\sim 2.3$  au), which is about five times larger than the expected stellar disk radius of the primary star,  $\sim 0.20$  mas  $\sim 100 R_{\odot} \sim 0.5$  au (Hillier et al. 2001). The first interferometric aperture-synthesis images of  $\eta$  Car A's distorted stellar wind zone with a spatial resolution of a few mas were reported by Weigelt et al. (2016) and Gravity Collaboration (2018). The measured line-of-sight (LOS) velocities of the obtained iso-velocity line images provide kinematical information about the wind zone.

In this paper we present the first Br $\alpha$  VLTI-MATISSE aperture-synthesis imaging of  $\eta$  Car's innermost wind region obtained during its February 2020 periastron passage. MATISSE is the new mid-infrared interferometry instrument of ESO's Very Large Telescope Interferometer (VLTI). In Sect. 2 we describe the observations. In Sect. 3 we present iso-velocity images of the stellar wind of the primary star reconstructed in several spectral channels distributed across the Br $\alpha$  line, in Sect. 4 we discuss the deformation of the primary wind by the WWC cavity, in Sects. 5 and 6 we compare the Br $\alpha$  and continuum observations of the primary stellar wind with the CMFGEN stellar wind model, and Sect. 7 summarizes our results.

## 2. Observations and data processing

The aperture-synthesis observations were performed over seven nights between 15 and 29 February 2020, close to periastron passage, which occurred on 18 February 2020. The orbital phases  $\phi$  on 15 and 29 February 2020 are  $\phi = 13.9987$  and

14.0056, respectively, if the orbital phase is calculated as described by Teodoro et al. (2016), where 14 is the cycle number. The average orbital phase of the observations is  $\phi = 14.0022$ . The  $uv$ -plane coverage of the observations and observing log are presented in Table A.1 and Fig. A.1, respectively.

The observations were performed with three configurations of the four auxiliary telescopes (ATs) of the ESO Very Large Telescope Interferometer (VLTI; Schöller 2007) and the new MATISSE interferometry instrument (multi-aperture mid-infrared spectroscopic experiment; Lopez et al. 2014, and in prep.; Matter et al. 2016; Petrov et al. 2018, 2020). The projected baseline lengths were in the range of 9.5–131 m. The reconstructed aperture-synthesis images have an angular resolution of  $\sim 6$  mas corresponding to  $\sim 14$  au at a distance of 2.3 kpc. All interferograms were recorded with a detector integration time (DIT) of 111 ms in the high spectral resolution mode (HR mode; spectral resolving power  $R=960$ ) in a narrow spectral band around the bright Br $\alpha$  4.052  $\mu$ m line. The observations of the night of 20–21 February 2020 in Table A.1 had very low quality because of dense, variable cirrus clouds and strong light absorption. These data were not used because a reliable calibration was not possible. All other data were reduced with the standard MATISSE Data Reduction Software (DRS), pipeline version 1.5.3<sup>1</sup>.

Each target or calibrator star observation consists of four data sets recorded at four different positions of the beam computing device (BCD; Millour et al. 2008) and two additional data sets recorded with two different BCD positions while taking photometric chopping data. To calibrate the interferometric transfer function (TF) and calculate TF-calibrated visibilities, we used the calibrator star  $\lambda$  Vel during observations with the compact configuration and  $\eta$  Car during the observations with the medium and large configuration (see details in Table A.1). The errors of the calibrated visibilities and closure phases were derived by calculating the standard deviation of the aforementioned six calibrated data sets. For the calculation of the total visibility error, we further took an additional error of 3%, which was derived from the variations in the atmospheric TF, into account (Petrov et al. 2020).

Figure B.1 presents an example of observations of  $\eta$  Car across the Br $\alpha$  line with the large AT configuration. The panels show the wavelength dependence of visibilities, closure phases, and Fourier phases (i.e., phases of the Fourier transform of the object, which can be derived from differential phases as discussed below). Baseline lengths (in the range of 55–129 m in this example) and position angles (PAs) are indicated in the panels. The lines with different colors are measurements taken with different configurations of the MATISSE BCD and therefore are taken at different times and different atmospheric conditions (separated by  $\sim 1$  min in time).

For image reconstruction, we used the wavelength-dependent visibilities, closure phases, and differential phases. Differential phases are very useful for image reconstruction if spectrally dispersed interferograms are recorded and a spectral line is resolved enough to get several resolved spectral channels (Petrov et al. 2007; Schmitt et al. 2009; Millour et al. 2011; Ohnaka et al. 2011, 2013; Mourard et al. 2015; Weigelt et al. 2016; Hone et al. 2017; Gravity Collaboration 2018). In this case, it is possible to derive the phase of the Fourier transform of the object in all spectral channels across a spectral line from the measured differential phases. The use of the differential phase for image reconstruction

<sup>1</sup> This software package is available from <ftp://ftp.eso.org/pub/dfs/pipelines/instruments/matisse/>

was first reported by Millour et al. (2011). Similar image reconstruction projects were reported by Ohnaka et al. (2011, 2013); Mourard et al. (2015); Weigelt et al. (2016); Hone et al. (2017); Gravity Collaboration (2018). This image reconstruction method is briefly summarized below.

In a small wavelength region around the  $\text{Br}\alpha$  line (in the case of our observations), the differential phase is approximately equal to the target Fourier phase (i.e., phase of the Fourier transform of the target) plus an unknown linear phase in wave number space. Therefore, the subtraction of this unknown linear phase from the differential phase provides the target Fourier phase needed for image reconstruction. The unknown linear phase is derived in the following way. From the visibilities and closure phases at continuum wavelengths on both sides outside of the line, a continuum image of the target is reconstructed (e.g., using IRBis; Hofmann et al. 2014) in the first step. This closure phase continuum image reconstruction provides the target Fourier phases in these two continuum wavelength regions. The difference between the differential phase and the Fourier phase (derived from the continuum reconstruction) is the above unknown linear phase in the two continuum regions. A linear fit to this unknown linear phase in the two continuum regions provides the unknown linear phase across the  $\text{Br}\alpha$  line necessary to derive the desired target Fourier phase in the  $\text{Br}\alpha$  line region.

The images presented in this paper were reconstructed from the visibilities, closure phases, and Fourier phases by using the MATISSE data reconstruction pipeline. Image reconstruction is described in Sect. 9.6 and D.2 in ESO's MATISSE Pipeline User Manual<sup>1</sup> (in image reconstruction tool `mat_cal_imarec`, which is an extension of `IRBis`). The start image of all reconstruction runs was a circular Gaussian, which was fit to the observed visibilities of  $\eta$  Car. The pixel grid used for the reconstructions was  $64 \times 64$  pixels corresponding to  $100 \times 100$  mas on the sky. A computed quality parameter of the reconstructions (called `qrec`; see Hofmann et al. 2014 for more details) allows the user to automatically find the reconstruction that agrees best with the observations. The images with the best quality parameters were obtained with the power 0.5 of the  $uv$  plane density weight and the Maximum Entropy regularization function (the cost function 3 method was used; for more details, see Hofmann et al. 2014, Sect. 9.6 and D.2 in ESO's MATISSE Pipeline User Manual<sup>1</sup> and Hofmann et al. 2021). The mean reduced  $\chi^2$  values of the squared visibilities, closure phases, and object Fourier transform phases of the reconstructed images are 2.22, 3.00, and 1.26, respectively. The mean residuals between squared visibilities, closure phases, and object Fourier transform phases derived from the interferograms and the same quantities derived from the reconstructed images are 0.0085,  $1.59^\circ$ , and  $0.79^\circ$ , respectively. In Figs. C.1–C.5, we compare all the observed visibilities, closure phases, and differential phases with the same interferometric quantities derived from the reconstructed images. This test is a useful standard method to investigate whether the visibilities and phases of observation and image reconstruction are in acceptable agreement.

### 3. The intensity distribution of $\eta$ Car's primary star stellar wind at several LOS velocities distributed across the $\text{Br}\alpha$ 4.052 $\mu\text{m}$ line

Figure 1 presents the velocity dependence of the reconstructed  $\text{Br}\alpha$  aperture-synthesis images of  $\eta$  Car (channel maps) at orbital phase  $\phi \sim 14.0022$ . The average LOS velocity of each image is

indicated in the images. At the top of Fig. 1, the continuum-normalized spectrum of the  $\text{Br}\alpha$  line and the surrounding continuum is shown as a function of both heliocentric vacuum wavelength and LOS velocity. In this spectrum, the flux is integrated over the entire  $600 \times 600$  mas field-of-view (FOV) of the MATISSE instrument. The FOV of each iso-velocity image is  $60 \times 60$  mas corresponding to  $138 \times 138$  au at a distance of 2.3 kpc. North (N) is up, and east (E) is to the left. All images were reconstructed with an angular resolution of 6.0 mas. The resolution beam diameter of 6.0 mas is shown in the  $863 \text{ km s}^{-1}$  image.

Figure 2 presents intensity cuts through the Fig. 1 images along the PA of  $120^\circ$ , which is the PA of the southeast (SE) extension in the  $-324 \text{ km s}^{-1}$  image (illustrated in Fig. 4). The cuts show a wide SE extension at negative velocities within the line and a northwest (NW) extension at positive velocities.

The images in Fig. 1 are normalized in the following way. The integrated intensity in the entire FOV of each iso-velocity image was scaled to the flux of the continuum-normalized spectrum. The velocities indicated in the images are intensity-weighted average velocities within the spectral channels (average channel widths  $\sim 170 \text{ km s}^{-1}$ ).

This normalization of the iso-velocity images to the spectrum is useful because it allows us to directly derive spectra of individual image regions, as demonstrated in Fig. 3. This figure presents five examples of spectra extracted at the five positions marked in Fig. 3 (bottom). The spectrum at the NW position is redder than the three spectra at the other off-axis positions, in agreement with the iso-velocity images. The spectrum extracted at the center pixel is completely different because a strong P Cygni absorption trough is seen at the negative velocities of  $-693$  to  $-165 \text{ km s}^{-1}$ .

In Fig. D.1, we additionally show the same images (Fig. 1), but normalized to unity in the brightness maximum of the images for comparison. These peak-normalized images are the primary output of the image reconstruction process. Contour lines are plotted at 20 and 98% of the peak intensity in order to highlight asymmetries in the images.

In the images in Fig. 1, two different types of structures can be seen, as in previous VLTI images reported by Weigelt et al. (2016) and Gravity Collaboration (2018). The first is a central, approximately circular continuum stellar wind intensity distribution of the primary star, which can be seen in all images (mainly in white, red, yellow, and green). The second is a much more extended  $\text{Br}\alpha$  line region of the stellar wind of the primary star (in green and blue) at several LOS radial velocities in the velocity range from  $-506$  to  $+313 \text{ km s}^{-1}$  (the faint, elongated primary stellar wind of the  $-506 \text{ km s}^{-1}$  image is better visible in the peak-normalized image in Fig. D.1).

The images in Fig. 1 reveal the following wavelength dependence. First, at the negative LOS velocities of  $-506$ ,  $-324$ , and  $-165 \text{ km s}^{-1}$ , the observed extended primary stellar wind is aspherical and less extended to the NW than in other directions. The WWC models reported by Madura et al. (2012, 2013) suggest that the observed elongated structure is caused by the collision of the high-density, low-velocity stellar wind of the primary star with the fast, low-density wind of the hot secondary star (see discussion in the next section). The low-density secondary stellar wind is probably not visible because it is too faint.

Second, the brightness of the innermost, circular region of the continuum primary stellar wind in Fig. 1 (in white, red, yellow, and blue) also depends on LOS velocity at negative velocities. This wavelength dependence suggests that we see P

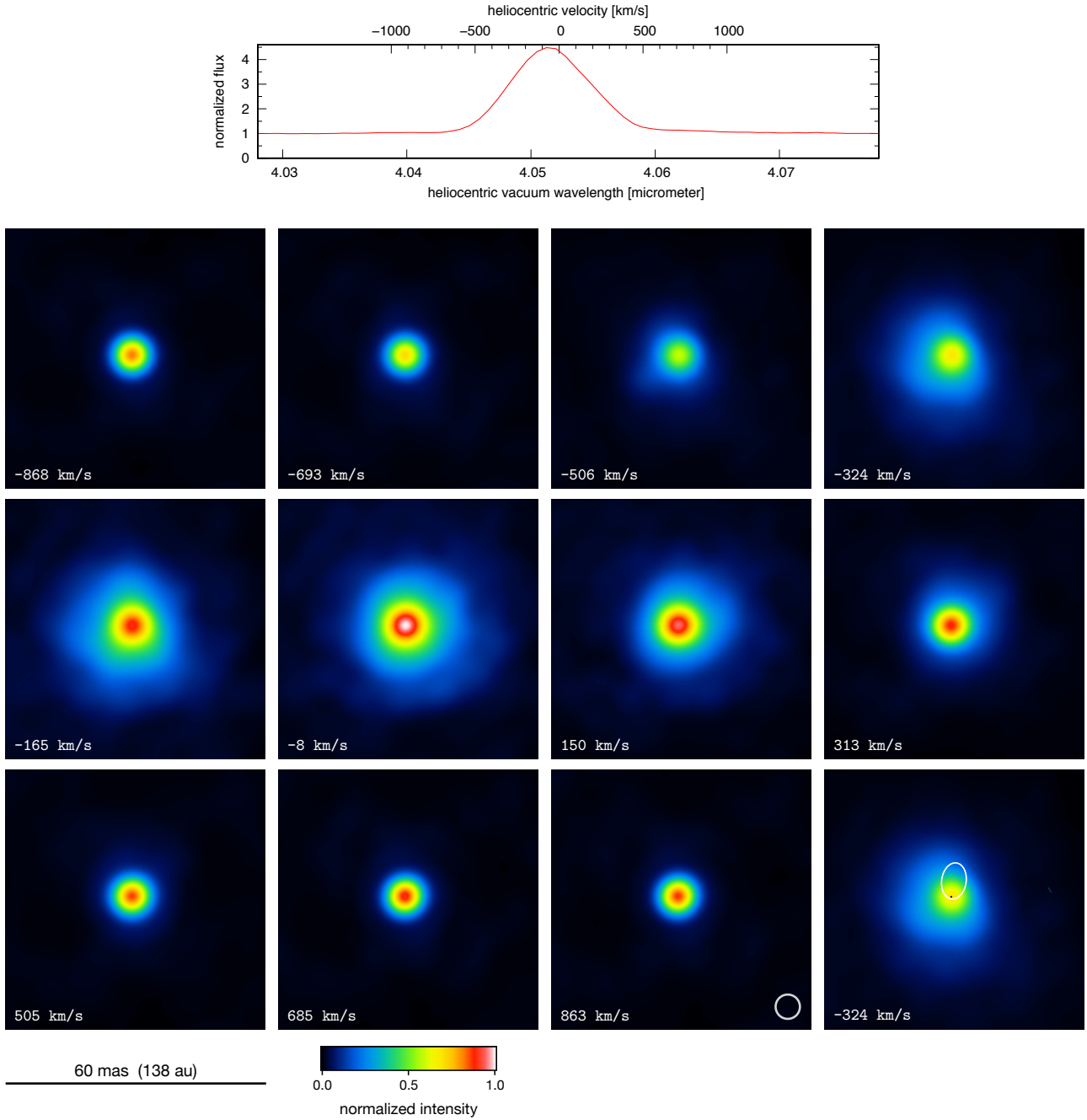


**Fig. 1.** Aperture-synthesis images of  $\eta$  Car observed in February 2020 at orbital phase  $\phi \sim 14.0022$ . *Top*: continuum-normalized Br $\alpha$  4.052  $\mu\text{m}$  flux (heliocentric vacuum wavelength; the small correction due to the system velocity of  $-8 \text{ km s}^{-1}$  (Smith 2004) has been neglected). *Bottom*: aperture-synthesis iso-velocity images of  $\eta$  Car’s compact continuum stellar wind of the primary star (central circular, compact region in mainly white, red, and yellow) and the much more extended emission line stellar wind of the primary star in several spectral channels distributed across the Br $\alpha$  4.052  $\mu\text{m}$  line (extended, irregular region in green and blue). The average LOS velocities of the spectral channels of the images are indicated in the images. The FOV of the images is  $60 \times 60 \text{ mas}$  or  $138 \times 138 \text{ au}$  for the adopted distance of 2.3 kpc (N is up, and E is to the left). The 6.0 mas diameter of the resolution beam is inserted in the  $863 \text{ km s}^{-1}$  image. The images show that the radius of the faintest visible primary stellar wind regions is  $\sim 26 \text{ mas}$  ( $\sim 60 \text{ au}$ ). *Bottom right*: comparison of the extension of the primary stellar wind (at an LOS velocity of  $-324 \text{ km s}^{-1}$ ) with a sketch of the orbit (white) of the secondary star relative to the primary star on the sky (e.g., the outer  $-8 \text{ km s}^{-1}$  Br $\alpha$  stellar wind radius is larger than the major axis of the binary orbit). The black dot indicates the position of the primary star. The major axis of the orbit is 30.9 au (Madura et al. 2012; orbit sketch adapted from Teodoro et al. 2016).

Cygni absorption in the central region of the images over a wide range of negative velocities, as reported in previous continuum-subtracted Br $\gamma$  2.166  $\mu\text{m}$  images (Weigelt et al. 2016). For example, the central primary stellar wind region of the  $-506$  and  $-324 \text{ km s}^{-1}$  images appear green and yellow, respectively,

which corresponds to lower brightness than the dark red central color in, for example, the  $-868$  and  $-8 \text{ km s}^{-1}$  iso-velocity images. This P Cygni absorption in the blue line wing can better be seen as a deep absorption trough in the spectrum shown in Fig. 3, as discussed above.



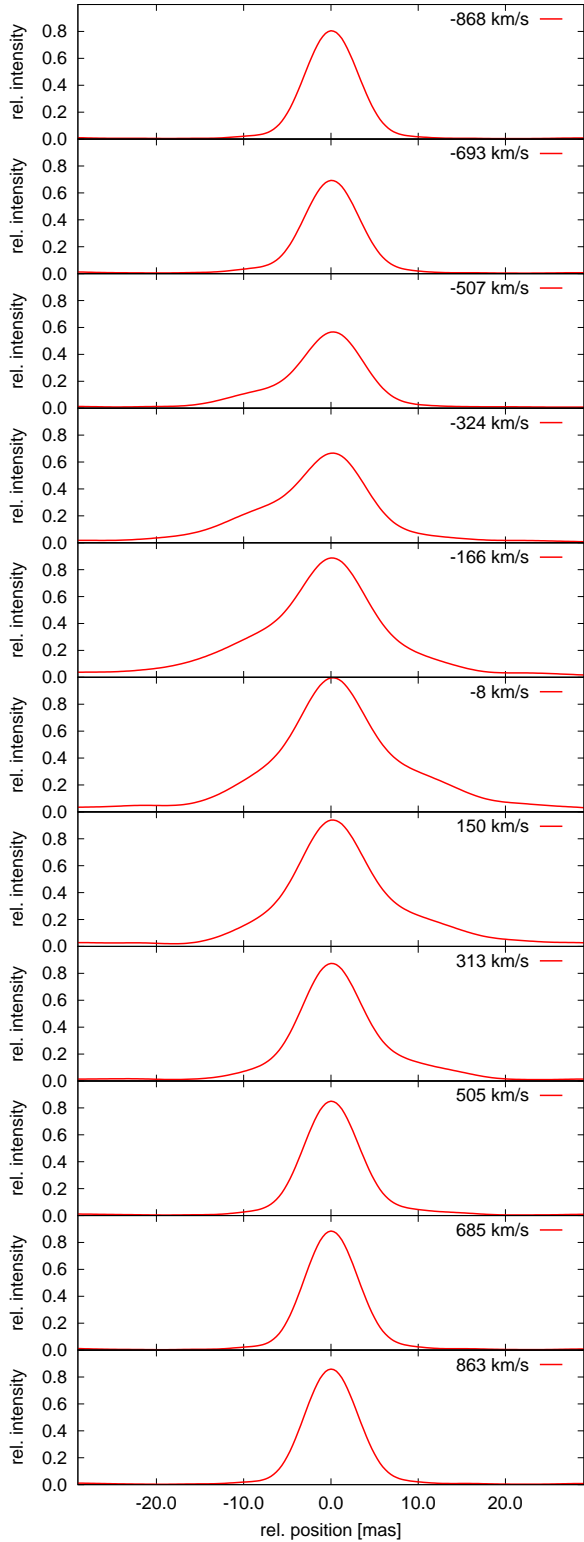


**Fig. 2.** Intensity cuts through the images in Fig. 1 along the PA of  $120^\circ$  (from SE to NW).

#### 4. Deformation of $\eta$ Car's primary stellar wind by the fast, low-density stellar wind of the hot companion star

To interpret the asymmetry of some of the images in Fig. 1, it is useful to compare these images with hydrodynamic models of

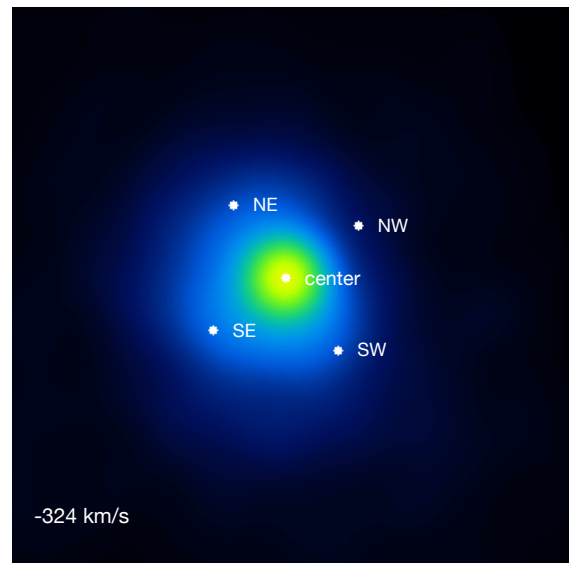
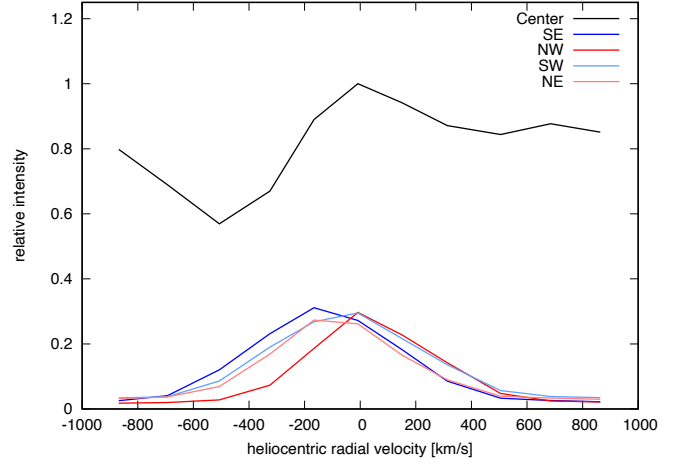


**Fig. 3.** Extraction of spectra from the 3D data cube in Fig. 1. *Top:* five spectra extracted at five selected positions from the 11 iso-velocity images in Fig. 1. *Bottom:* five positions chosen in the images in Fig. 1 to extract five spectra (top) from the 3D data cube of Fig. 1, shown by the dots at center, NE, SE, SW, and NW (same color table as in Fig. 1).

the WWC (Okazaki et al. 2008; Madura et al. 2012, 2013; Russell et al. 2016).

Figure 4 (top) presents the orientation of a 3D WWC cavity model as seen on the sky at orbital phase  $\phi = 0.003$  (adapted from Fig. 3 in Madura & Groh 2012). This figure illustrates the observer's LOS view of the curved shape of the WWC cavity in the primary stellar wind carved out by the secondary stellar wind (N is up, and E is to the left). This LOS view presentation is important for the following discussion because it illustrates the expected LOS velocity distribution on the curved WWC cavity surface seen by the observer. The cavity colors indicate the distance of structures on the curved WWC cavity surface from the central stars (i.e., geometric shape, not density or intensity). Dark purple indicates surface structures at large radii of about 75–125 au while green indicates regions near the apex of the wind collision zone (see Madura & Groh 2012 for more details).

The four arrows in Fig. 4 (top) illustrate the motion direction of cavity surface structures in the outer region of the cavity, which move outward from the apex (however, in the inner region, the velocity field is more complicated). The light emitted from

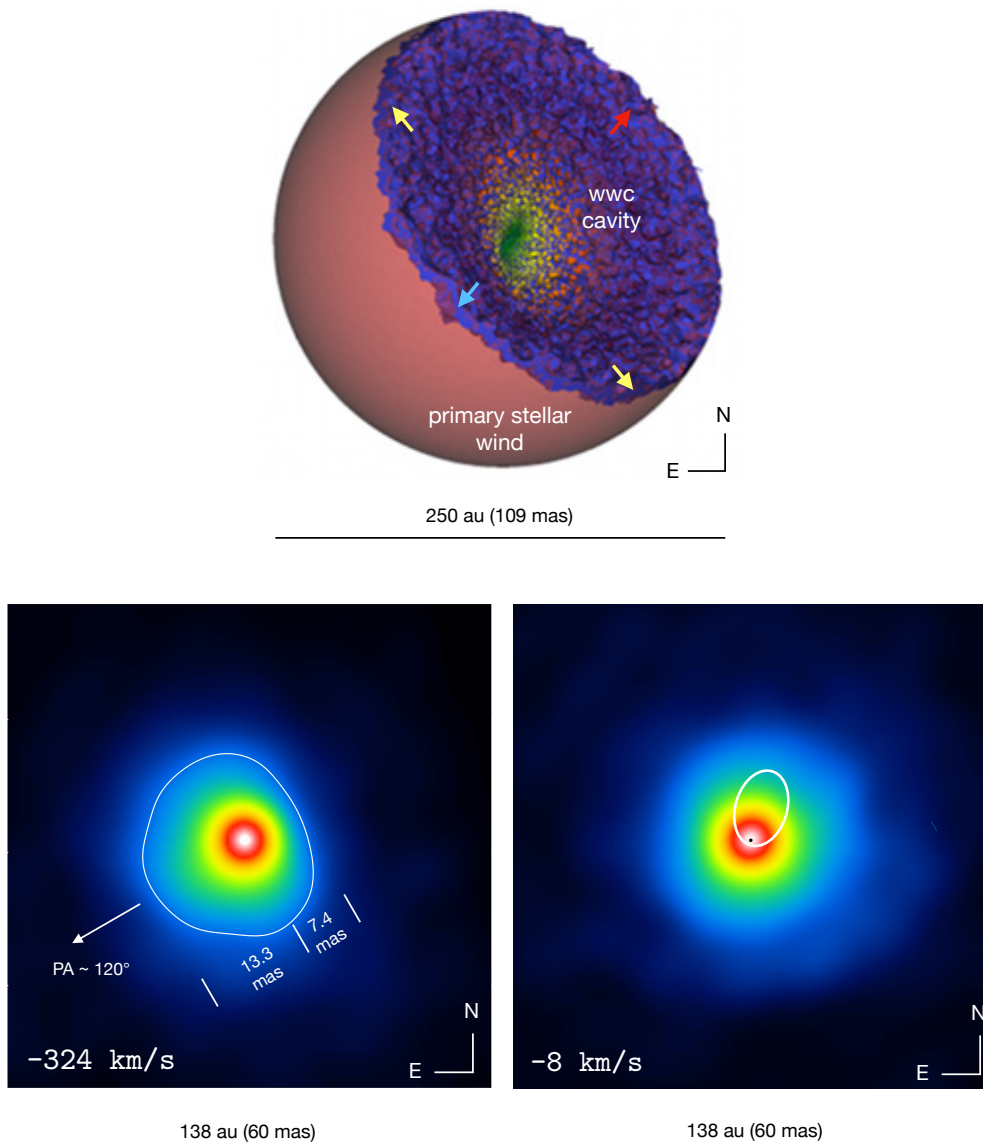


**Fig. 4.** Inclined WWC cavity of  $\eta$  Car and its distorted stellar wind of the primary star. *Top:* geometric curved shape and orientation of a 3D hydrodynamical simulation of  $\eta$  Car’s WWC cavity (adapted from Fig. 3 in Madura & Groh 2012). The figure shows the LOS view of the geometric shape of the inclined WWC cavity surface, illustrating the orientation of the cavity shape as seen on the sky at orbital phase  $\phi=0.003$ . The surface of the WWC cavity is color-coded to radius. The dark purple indicates WWC gas at radii of about 75 to 125 au from the primary star. Green indicates gas near the apex of the WWC cavity at a distance of less than 15 au from the primary. The arrows indicate the motion directions of the gas on the cavity surface. The model illustrates that the observer is looking almost parallel along the SE wall of the cavity leading to blue-shifted light emitted from this region. *Bottom left:*  $\eta$  Car’s aperture-synthesis image at an LOS velocity of  $-324 \text{ km s}^{-1}$  with a contour line at 20% of the peak intensity (from Fig. D.1), which illustrates the asymmetry along PA  $\sim 120^\circ$ . The blue-shifted light with an LOS velocity of  $-324 \text{ km s}^{-1}$  is more extended to the SE than to the NW, as expected from the orientation of the model of the WWC cavity (top). *Bottom right:* comparison of the extension of the primary stellar wind (at an LOS velocity of  $-8 \text{ km s}^{-1}$ ; from Fig. 1) with the binary orbit (white) of the secondary star relative to the primary star on the sky. The black dot indicates the position of the primary star. The major axis of the orbit is 30.9 au (Madura et al. 2012; orbit adapted from Teodoro et al. 2016).

the SE cavity surface region is expected to be blue-shifted because we are looking almost parallel along the cavity surface in the SE. However, the observed velocity field is more complicated because the observer sees the sum of the light emitted from the surface of the WWC cavity and the light from the undisturbed primary stellar wind, as discussed below. The low-density secondary stellar wind is not visible because it is too faint. The outer faint regions of the undisturbed primary star stellar wind and the WWC cavity are more extended than shown in Fig. 4 (Madura et al. 2012, 2013; Groh et al. 2012a; Russell et al. 2016).

The phase-dependent orientation of the curved wind collision cavity on the sky shown in Fig. 4 (top) can roughly explain the discussed SE-NW asymmetry of the images at negative velocities ( $-506$ ,  $-324$ , and  $-165 \text{ km s}^{-1}$ ). This asymmetry was also seen at previous observations at other orbital phases (Weigelt et al. 2016; Gravity Collaboration 2018).

Figure 4 (bottom) illustrates the shape of this asymmetry at the 20% contour level. The PA of the SE-NW asymmetry is  $\sim 120^\circ$ . Along this PA, the SE extension is  $\sim 13.3 \text{ mas}$ , whereas the NW extension is only  $7.4 \text{ mas}$  (i.e., an asymmetry ratio of almost two).

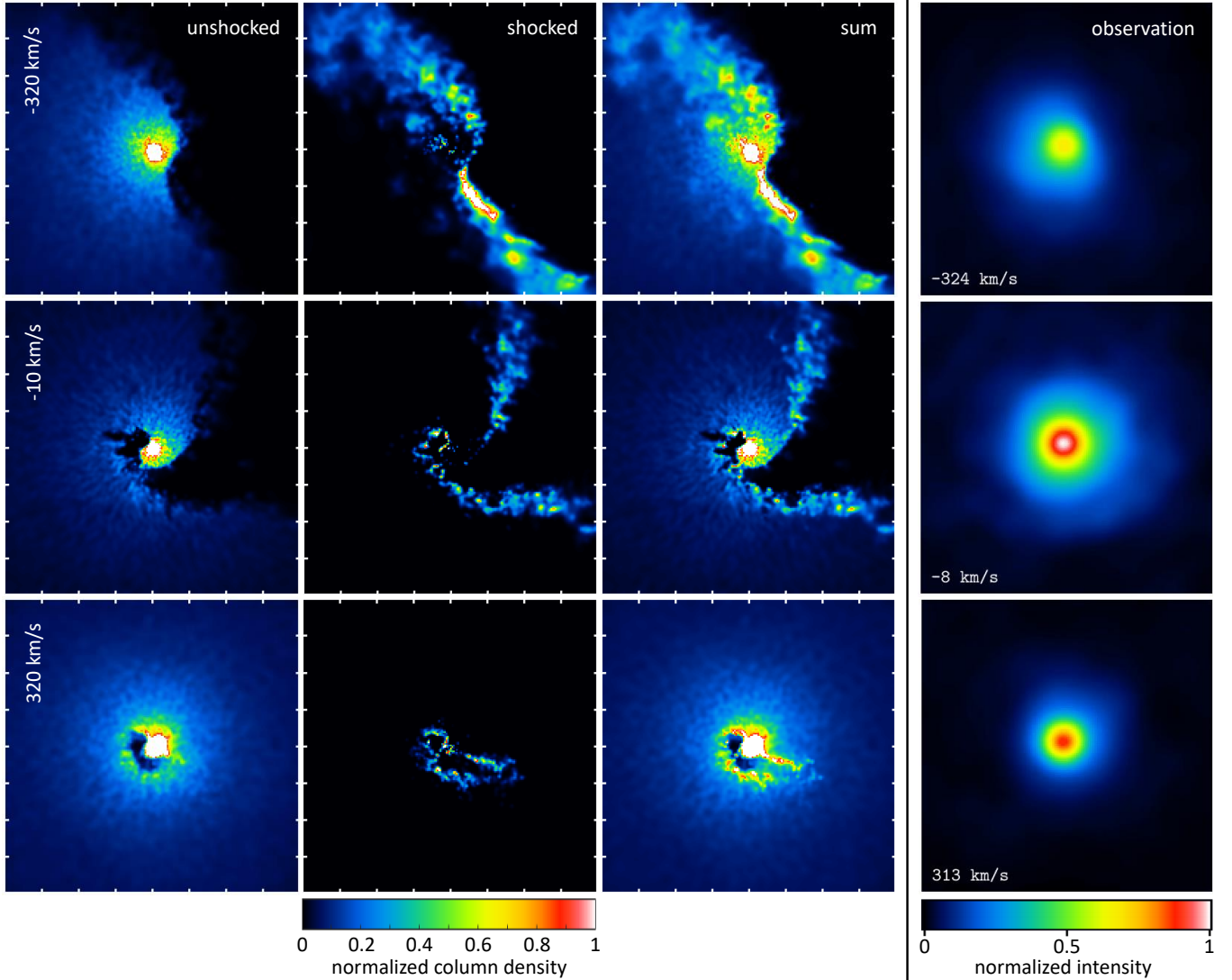


**Fig. 5.** Comparison of  $\eta$  Car images (*fourth column*) from Fig. 1 with 3D hydrodynamic simulations of LOS column density distributions of  $\eta$  Car’s distorted stellar wind and WWC zone of the primary star only for the three LOS velocities of  $-320$ ,  $-10$ , and  $+320$   $\text{km s}^{-1}$ . The model images show the LOS view as seen on the sky at orbital phase  $\phi=0.014$ , i.e., very close to the phase of 0.0022 of the observations. *Top*: LOS velocity of  $-320$   $\text{km s}^{-1}$ . *Middle*: LOS velocity of  $-10$   $\text{km s}^{-1}$ . *Bottom*: LOS velocity of  $+320$   $\text{km s}^{-1}$ . *From left to right* are shown the un-shocked wind column density distribution, shocked wind column density distribution, the model sum of both (shocked plus un-shocked), and the observed images at similar LOS velocities. The FOV of all model column density maps and observed images is  $60 \times 60$  mas or  $138 \times 138$  au for the adopted distance of 2.3 kpc. N is up, and E is to the left.

Even if this SE-NW asymmetry can approximately be explained by the expected velocity field on the cavity surface, the total 3D velocity field of the wind zone is more complex, as it contains contributions from three velocity components. The first is the velocity field on the WWC cavity surface. The second is the velocity field of the undisturbed primary stellar wind outside and behind the WWC cavity. The primary star stellar wind is seen through the partially transparent WWC cavity surface, as the images in Fig. 1 suggest. The third is the velocity field of the wind of the primary star immediately below the cavity surface and the primary wind material accelerated by the interaction with the fast ( $\sim 3000$   $\text{km s}^{-1}$ ), low-density stellar wind of the secondary star because the cavity wall is not thin, but consists of shocked material from each star on its side, each having a different wind speed.

To discuss this velocity distribution of the wind in more detail, Fig. 5 presents models of the LOS column density

distributions of  $\eta$  Car’s distorted primary stellar wind and WWC for LOS velocities of  $-320$ ,  $-10$ , and  $+320$   $\text{km s}^{-1}$ . These models are 3D smoothed particle hydrodynamics (SPH) simulations computed with the code described by Russell et al. (2016) (see also Madura et al. 2013 and Okazaki et al. 2008 for key features). The stellar, wind, and orbital parameters are summarized in Table 1 in Russell et al. (2016), with the highest primary mass-loss rate  $\dot{M}_1 = 8.5 \times 10^{-4} M_{\odot} \text{ yr}^{-1}$  used here. To compute the LOS column density distributions in Fig. 5, the parameters of the binary orbit derived by Madura et al. (2012) were adopted. This orbit shows that the orbital axis is closely aligned with the 3D polar axis of the Homunculus nebula.

The column density distributions in Fig. 5 do not afford a direct comparison of the models to the observed intensity distribution from Fig. 1; this would require 3D radiative transfer calculations on the hydrodynamic output, which are beyond the scope of this work. However, the column density distributions

show where the primary wind material is located for different LOS velocities as a result of the WWC, and thus provide a basis for explaining the observed asymmetries, for example, the small extension of the  $-324 \text{ km s}^{-1}$  image (Fig. 1) to the NW, as discussed below.

First, Fig. 5 (top row) presents from left to right the  $-320 \text{ km s}^{-1}$  LOS column density distribution of the un-shocked primary stellar wind, the shocked wind, the sum of shocked and un-shocked wind, and the observed  $-324 \text{ km s}^{-1}$  image from Fig. 1, which has a much lower spatial resolution (6 mas) than the models. The column density distributions show that there is essentially no  $-320 \text{ km s}^{-1}$  blue-shifted wind material in the outer NW region because of the WWC. Therefore, the sum of both  $-320 \text{ km s}^{-1}$  wind components is less extended to the NW than to the SE, which is consistent with the observed  $-324 \text{ km s}^{-1}$  image. Second, Fig. 5 (top, middle-left) presents a wide NE-SW extension of the shocked wind that can explain the NE-SW extension of the observed  $-324 \text{ km s}^{-1}$  image.

Third, Fig. 5 (middle row) presents the same types of column density maps as shown in the top row, but for the low velocity of  $-10 \text{ km s}^{-1}$  (at the same orbital phase). These  $-10 \text{ km s}^{-1}$  column density maps have the interesting advantage that the leading and trailing arms of the WWC cavity can be seen, which helps to better understand the structures of WWC arms at other velocities. The model maps are less asymmetric than the  $-324 \text{ km s}^{-1}$  maps.

Fourth, Fig. 5 (bottom row) presents the same types of maps as shown in the other rows, but for the LOS velocity of  $+320 \text{ km s}^{-1}$  for comparison. The model maps are less asymmetric than the  $-320 \text{ km s}^{-1}$  maps, which is consistent with the observed image.

To study  $\eta$  Car's wind zone in more detail in the future, we will have to perform more aperture-synthesis observations with higher spectral resolution and better  $uv$  coverage and, in particular, at many different orbital phases and in different lines.

## 5. Comparison of the Br $\alpha$ stellar wind of the primary star with the CMFGEN stellar wind model

Due to its extended wind, we cannot use a standard limb-darkening law to interpret the observations of  $\eta$  Car. Instead we utilized a spherically symmetric non-local thermodynamic equilibrium (non-LTE) line-blanketed wind model of the primary star and its wind, which was generated using the non-LTE code CMFGEN (Hillier & Miller 1998; Hillier et al. 2001).

We adopted the following model parameters: radius  $R_{\text{core}} = 120 R_{\odot}$ ; radius  $R_{\tau=2/3} = 742 R_{\odot}$ ; effective temperature  $T_{\text{eff}(\tau=2/3)} = 9470 \text{ K}$ ; velocity  $V_{\tau=2/3} = 357 \text{ km s}^{-1}$ ; luminosity  $L = 4.0 \times 10^6 L_{\odot}$ ; mass-loss rate  $\dot{M} = 8.0 \times 10^{-4} M_{\odot} \text{ yr}^{-1}$ ; terminal velocity  $V_{\text{inf}} = 420 \text{ km s}^{-1}$ ; and clumping volume filling factor = 0.1.

Figure 6 presents a comparison of two of the iso-velocity images from Fig. 1 with the intensity center-to-limb variation (CLV) in the above CMFGEN model of the primary stellar wind. The  $-8 \text{ km s}^{-1}$  line image and the corresponding normalized CMFGEN intensity distribution in Fig. 6 (top) show that the radius of the intensity distribution of the primary stellar wind is huge ( $\sim 60 \text{ au}$ , as Fig. 7 shows more clearly) at the faintest intensities seen. Figure 6 (bottom) presents, for comparison, the less extended  $+863 \text{ km s}^{-1}$  near-continuum primary stellar wind image and the corresponding CMFGEN model CLV. The angular resolution of the two model CLV functions is degraded to

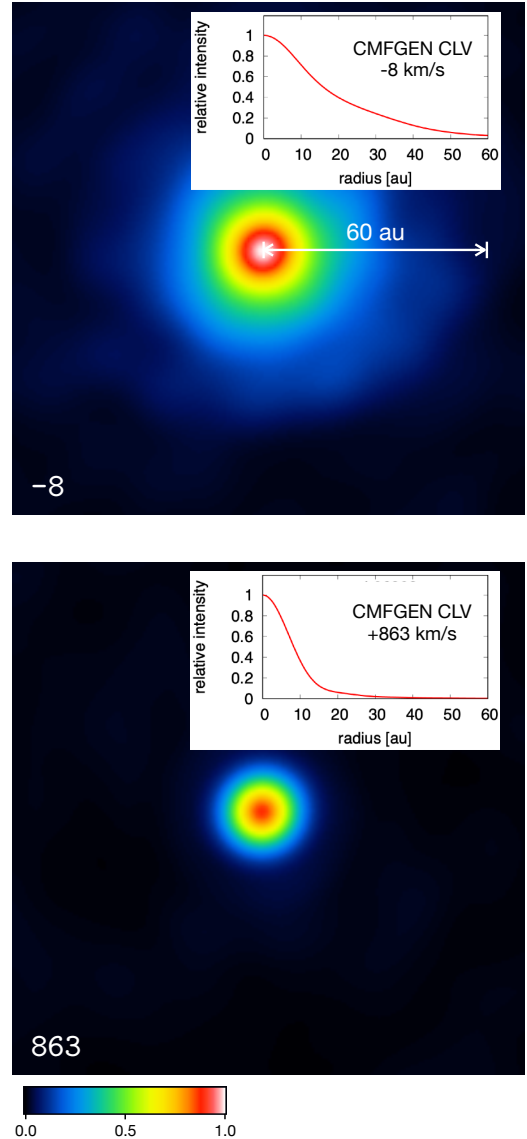


**Fig. 6.** Comparison of the intensity distribution of two images from Fig. 1 ( $-8$  and  $+863 \text{ km s}^{-1}$ ) with the intensity CLV of the stellar wind CMFGEN model. The model CLVs are convolved with a point spread function with 6 mas diameter to match the resolution of the observed images. *Top:* Br $\alpha$  stellar wind image of the primary star at the velocity of  $-8 \text{ km s}^{-1}$  and the corresponding CMFGEN model. *Bottom:* continuum  $+863 \text{ km s}^{-1}$  image of the stellar wind of the primary star and the corresponding CMFGEN model.

an angular resolution of 6.0 mas (FWHM) to match the spatial resolution of the observed images.

Figure 7 compares the azimuthally averaged, 1D intensity CLVs of all reconstructed images in Fig. 1 with the corresponding CMFGEN model CLVs. The angular resolution of the model CLVs is degraded to an angular resolution of 6 mas (FWHM) to match the spatial resolution of the observed images. The velocities in the panels are velocities averaged over spectral regions that have the same spectral widths as in the observations (Fig. 1). Before we calculated these average velocities, we adapted the spectral resolution of the model CLV to the spectral resolution  $R = 960$  of the observations.

Figure 7 shows that the model CLVs have a similar extension as the observed images. At the faintest visible intensities, both the model and observed radii are about 60 au. However,



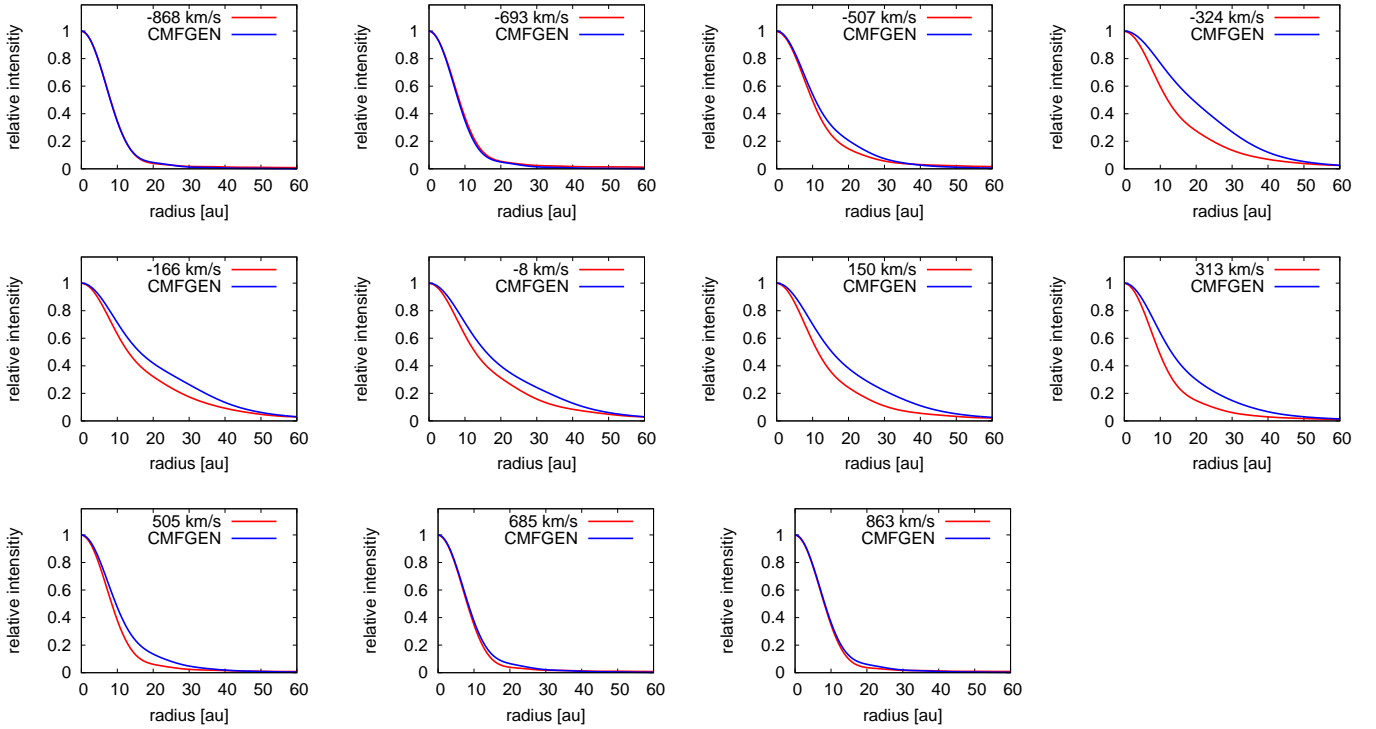


**Fig. 7.** Comparison of the azimuthally averaged CLV of the intensity distributions of the images in Fig. 1 (red line) with the predicted CLV of the intensity distributions of the CMFGEN model (blue line). The model CLV functions are convolved with the radial profile of an airy disk with a FWHM diameter of 6 mas to match the spatial resolution of the observed CLVs.

the intensities of the observed CLVs are lower than the model intensities at most radii. The reason for this difference is not known.

The CMFGEN model is a single-star stellar wind model, in which WWC is not taken into account. Therefore, we do not expect a perfect agreement between the CMFGEN model and the observation.

It is not clear whether the distortion by the WWC is so strong that the WWC is the main reason for the difference between the model and observations. It is also possible that the parameters chosen for the calculation of the above CMFGEN model are the main reason for the difference between the model and observations.

To illustrate the dependence of the model CLV shape on the model parameters, we present two additional CMFGEN models in Fig. E.1. These two examples show that a mass-loss rate of  $4.0 \times 10^{-4} M_{\odot} \text{ yr}^{-1}$  leads to a lower and more curved CLV than the mass-loss rate  $5.0 \times 10^{-4} M_{\odot} \text{ yr}^{-1}$ . These examples in Fig. E.1 illustrate that the mass-loss rate is one of the parameters that is able to change the curvature of the model CLV. CMFGEN stellar wind models also allow for the presence of clumping within the wind using a volume-filling factor approach. A volume filling factor of 0.1 is assumed in all presented models.

As we have discussed already, it is not known whether the difference between the model CLVs and the observed CLVs is mainly caused by the phase-dependent WWC or the assumed CMFGEN model parameters. To investigate this question, we plan to perform new observations of the CLV shape in 2022 at a near-apastron phase when the WWC cavity has moved to the outer region of the primary star wind. The comparison of the 2020 periastron and 2022 apastron observations will allow us to study the phase dependence of the WWC.

## 6. Comparison of the continuum stellar wind of the primary star with the CMFGEN stellar wind model

To derive the diameter of the continuum stellar wind of the primary star and compare the observations with the CMFGEN model, we fit the measured continuum visibilities with the visibilities of the CMFGEN model presented at the beginning of Sect. 5.

Figure 8 (top) presents the interferometric visibilities (filled circles with error bars) measured in the continuum region beyond the  $\text{Br}\alpha$  line. To compute these visibilities we chose the visibilities in the spectral continuum channels of  $4.028\text{--}4.031 \mu\text{m}$  and  $4.072\text{--}4.075 \mu\text{m}$  because these regions are as far away from the  $\text{Br}\alpha$  line as our data permit and are free from strong lines. These visibilities allow us to study the shape and FWHM of the CLV of the primary stellar wind in the continuum and its deviation from circular symmetry.

Figure 8 (bottom) presents the normalized intensity distribution versus radius of this CMFGEN stellar wind model. To compare the observed visibilities with the model prediction, we derive the model visibilities of the CMFGEN model CLV by Fourier transforming the 2D model CLV and fitting the obtained model visibilities to the observed visibilities.

The model CLV in Fig. 8 (bottom) is the wavelength-averaged model CLV averaged over the same continuum region as used to derive the observed visibilities. Before averaging, the spectral resolution of the model was adapted to the spectral resolution of the observations (see Sect. 5). In both cases, we computed the average over the continuum wavelength regions of  $4.028\text{--}4.031 \mu\text{m}$  and  $4.072\text{--}4.075 \mu\text{m}$ .

Figure 8 (top, red line) shows the derived CMFGEN model visibility function obtained for the diameter rescaling factor of

**Table 1.** Interferometric observations of the elongation of  $\eta$  Car’s primary continuum stellar wind.

Elongation axis ratio	PA of major axis	Orbital phase $\phi$	Reference
$1.25 \pm 0.05$	$138 \pm 7^\circ$	10.7–10.9	van Boekel et al. 2003
$1.18 \pm 0.10$	$120 \pm 15^\circ$	11.27–11.30	Weigelt et al. 2007
$1.07 \pm 0.14$	$159 \pm 47^\circ$	12.89–12.92	Weigelt et al. 2016
$1.06 \pm 0.05$	$130^\circ$	13.28&13.51	Gravity collaboration et al. 2018
$1.08 \pm 0.02$	$123_{-5}^{+6^\circ}$	14.0022	This work

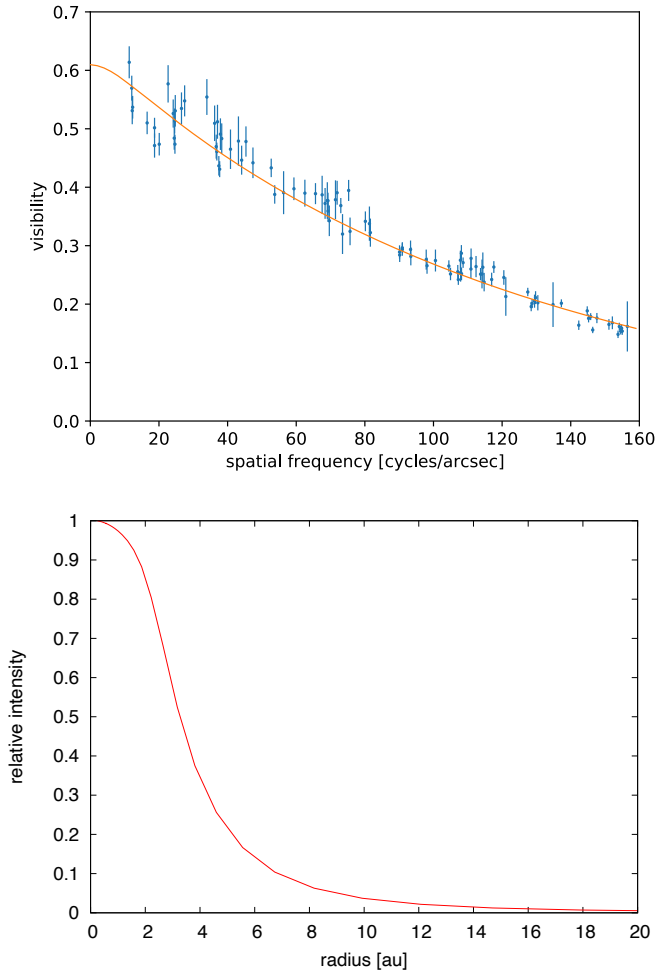


**Fig. 8.** Comparison of  $\eta$  Car’s observed and model continuum visibilities. *Top:* observed  $\eta$  Car visibilities in the continuum near  $\text{Br}\alpha$  versus spatial frequency, and the visibility curve of the rescaled CMFGEN model (red line; rescaling factor = 1.0046; see text). *Bottom:* CMFGEN model intensity CLV of the  $\eta$  Car primary stellar wind in the continuum near  $\text{Br}\alpha$ . The FWHM diameter of the rescaled model is 6.54 au (or 2.84 mas at a distance of 2.3 kpc).

1.0046. This small rescaling factor is required to get the best fit. The  $1\text{-}\sigma$  fit error is  $\sim 1.0\%$ . The fit is performed with the Python Markov chain Monte Carlo (MCMC) software *emcee* (Foreman-Mackey et al. 2013b,a). The corresponding posterior distributions of the fit parameters and their errors are presented in Fig. F.1.

The FWHM diameter of the original CMFGEN model (without rescaling) in the above  $\text{Br}\alpha$  continuum region is 6.507 au, and the rescaled model CLV has a FWHM diameter of  $6.507 \text{ au} \times 1.0046 = 6.537 \text{ au}$ . Therefore, with this visibility

fit, we obtain a measured CMFGEN model fit FWHM diameter of the continuum primary stellar wind intensity distribution of  $\sim 6.537 \text{ au} \pm 1.0\%$  ( $1\sigma$  error) corresponding to 2.842 mas ( $\pm 1.0\%$ ) for a distance of 2.3 kpc. However, this 1.0% fit error does not yet include the error that results from the diameter uncertainties of the diameters of the interferometric calibrator stars. Including these calibrator star uncertainties, we estimate the total error to  $\pm 2.15\%$  (see Appendix F). Therefore, our final CMFGEN model fit FWHM diameter of the primary stellar wind intensity distribution (in the  $4.028\text{--}4.031 \mu\text{m}$  and  $4.072\text{--}4.075 \mu\text{m}$  continuum) is  $6.54 \text{ au} \pm 2.15\%$  or  $6.54 \pm 0.14 \text{ au}$ , which corresponds to  $2.84 \pm 0.06 \text{ mas}$  for a distance of 2.3 kpc.

Finally, the 2D distribution of the observed visibilities allows us to investigate the aspherical shape of the continuum primary stellar wind revealed by spectroscopic HST observations (Smith et al. 2003) and interferometric observations (van Boekel et al. 2003; Weigelt et al. 2007, 2016; Gravity Collaboration 2018) listed in Table 1. Smith et al. (2003) first discovered that the stellar wind of  $\eta$  Car is latitude-dependent and the major axis of the stellar wind and the major axis of the Homunculus on the sky are aligned. These measurements were possible because the spectroscopic observations of scattered light from different regions of the Homunculus provided a rare opportunity to observe the spectrum of a star from more than one direction.

To measure the elongation of the intensity distribution of the continuum stellar wind, we fit (using the aforementioned MCMC *emcee* software) the observed 2D visibility distribution with an elliptically stretched 2D version of the model visibility, which has a radial CMFGEN model CLV profile. The corresponding posterior distributions of the fit parameters and their errors are presented in Fig. F.4. Our best  $\chi^2$  fit provides an ellipse axis ratio of  $1.08 \pm 0.02$  ( $1\sigma$  error) and a PA of the major axis of the ellipse of  $123_{-5}^{+6^\circ}$ , which means that the major axis is roughly aligned with the projected Homunculus axis (PA  $\sim 132^\circ$ ; Davidson & Humphreys 1997; Davidson et al. 2001; Smith 2006). The reported elongation measurements (Table 1) can be explained by aspherical stellar wind models with enhanced mass loss along the polar direction as proposed, for example, by Owocki et al. (1996, 1998) or Maeder & Desjacques (2001) for stars rotating close to their critical speed (wind collision studies by Madura indicate that the Homunculus axis is approximately aligned with the primary polar axis; Madura et al. 2012, 2013). Other studies suggest that the stellar wind shape may be influenced by the WWC (Groh et al. 2010a, 2012b; Mehner et al. 2012). More observations at various orbital phases are required in the future to improve our knowledge on the aspherical shape and the phase dependence of the primary stellar wind.

## 7. Summary and conclusions

We have presented the first VLTI-MATISSE  $\text{Br}\alpha$  4.052  $\mu\text{m}$  aperture-synthesis images, which show the dependence of

$\eta$  Car's 2D wind intensity distribution on wavelength or LOS velocity in several spectral channels distributed across the Br $\alpha$  line. The observations were performed with all three configurations of the VLTI (baseline range 9.5–131 m) at orbital phase  $\phi \sim 14.0022$ . We obtained the following results:

- The reconstructed iso-velocity images show both the compact continuum and the much more extended Br $\alpha$  intensity distribution of the stellar wind of the primary star  $\eta$  Car A. The reconstructed images have a spatial resolution of 6.0 mas or 14 au. The extension of the observed Br $\alpha$  primary stellar wind has a radius of  $\sim 60$  au ( $\sim 26$  mas) at the faintest visible outer region.
- The wavelength dependence of the wind in the inner 6 mas strongly suggests that we see P Cygni absorption in the central 6 mas region of the images in a wide range of negative velocities. This P Cygni absorption is also seen as a wide absorption trough in the presented spectrum extracted from the 3D data cube of the iso-velocity images.
- In spectral channels with high negative LOS velocities ( $-506$ ,  $-324$ , and  $-165$  km s $^{-1}$ ), the image intensity distributions are asymmetric and more extended to the SE than to the NW.
- The comparison of the iso-velocity images with hydrodynamic models of the wind collision region can explain the observed SE-NW asymmetry of the images. This asymmetry suggests that the system axis of the wind collision region is inclined with respect to our LOS and that we are looking almost parallel along the SE wall of the wind collision cavity.
- We compare the azimuthally averaged, 1D intensity CLVs of all reconstructed Br $\alpha$  images with the corresponding CMFGEN model CLVs. The differences between the model and observations may be caused by the wind collision, which is able to change both the shape and the kinematics of the primary stellar wind.
- The diameter of the continuum stellar wind of the primary star is measured by fitting a CMFGEN model CLV to the observed visibilities. We measure a CMFGEN fit FWHM diameter of  $2.84 \pm 0.06$  mas, which corresponds to  $6.54 \pm 0.14$  au for a distance of 2.3 kpc.
- To study the aspherical shape of the stellar primary wind, we measured the elongation of the intensity distribution of the continuum primary stellar wind. We fit the observed 2D visibility distribution with an elliptically stretched 2D version of the model visibility, which has a radial CMFGEN model CLV profile. Our fit result provides an ellipse axis ratio of  $1.08 \pm 0.02$  and a PA of the major axis of the ellipse of  $123^{+60}_{-5}$ , which is roughly aligned with the PA of the projected Homunculus axis.

The VLTI aperture synthesis imaging provides intensity and velocity distributions with milliarcsecond spatial resolution. Therefore, they can be used to test and refine hydrodynamical models of  $\eta$  Car's phase-dependent interacting winds. VLTI-GRAVITY and VLTI-MATISSE allow us to perform such observations in many different spectral lines in the  $K$ ,  $L$ ,  $M$ , and  $N$  bands. Future observations at many orbital phases are required to study the WWC in detail.

**Acknowledgements.** MATISSE was designed, funded and built in close collaboration with ESO, by a consortium composed of institutes in France (J.-L. Lagrange Laboratory – INSU-CNRS – Côte d'Azur Observatory – University of Côte d'Azur), Germany (MPIA, MPIfR and University of Kiel), the Netherlands (NOVA and University of Leiden), and Austria (University of Vienna). We thank all ESO colleagues for the excellent collaboration. This work has been supported by the French government through the UCAJEDI Investments in the Future project managed by the National research Agency (ANR) with

the reference number ANR-15-IDEX-01. The Konkoly Observatory and Cologne University have also provided some support in the manufacture of the instrument. K.O. acknowledges the support of the Agencia Nacional de Investigación y Desarrollo (ANID) through the FONDECYT Regular grant 1180066. S.K. and A.K. acknowledge support from an STFC Consolidated Grant (ST/V000721/1) and ERC Starting Grant (Grant Agreement No. 639889). The research of J.V. and M.H. is supported by NOVA, the Netherlands Research School for Astronomy. T.H. acknowledges support from the European Research Council under the Horizon 2020 Framework Program via the ERC Advanced Grant Origins 83 24 28. A.G. acknowledges support from the European Research Council (ERC) under the European Union's Horizon 2020 research and innovation programme under grant agreement No 695099 (project CepBin). P.A. acknowledges support from the Hungarian NKFIH OTKA grant K132406, and from the European Research Council (ERC) under the European Union's Horizon 2020 research and innovation programme under grant agreement No 716155 (SACCRED). A.F.J.M. is grateful for financial aid from NSERC (Canada) and FQRNT (Quebec). J.S.B. acknowledges the support received from the UNAM PAPIIT project IA 101220 and from the CONACyT project 263975. N.D.R. acknowledges some support from HST-GO programs 15611 and 15992. C.M.P.R. acknowledges support from NASA grants with *Chandra* award number GO0-21006A and NICER award numbers 80NSSC19K1451 and 80NSSC19K1459. A.D. thanks support from FAPESP #2019/02029-2. F.N. acknowledges FAPESP for support through proc. 2017/18191-8. This research has made use of the services of the ESO Science Archive Facility. This publication makes use of the SIMBAD database operated at CDS, Strasbourg, France. We thank the referee for helpful suggestions.

## References

- Bourges, L., Mella, G., Lafrasse, S., et al. 2017, *VizieR Online Data Catalog: II/346*
- Clementel, N., Madura, T. I., Kruip, C. J. H., & Paardekooper, J.-P. 2015, *MNRAS*, **450**, 1388
- Corcoran, M. F. 2005, *AJ*, **129**, 2018
- Corcoran, M. F., Ishibashi, K., Davidson, K., et al. 1997, *Nature*, **390**, 587
- Corcoran, M. F., Ishibashi, K., Swank, J. H., & Petre, R. 2001, *ApJ*, **547**, 1034
- Corcoran, M. F., Liburd, J., Morris, D., et al. 2017, *ApJ*, **838**, 45
- Cruzalèbes, P., Petrov, R. G., Robbe-Dubois, S., et al. 2019, *MNRAS*, **490**, 3158
- Damineli, A. 1996, *ApJ*, **460**, L49
- Damineli, A., Conti, P. S., & Lopes, D. F. 1997, *New Astron.*, **2**, 107
- Damineli, A., Stahl, O., Kaufer, A., et al. 1998, *A&AS*, **133**, 299
- Davidson, K. 1997, *New Astron.*, **2**, 387
- Davidson, K., & Humphreys, R. M. 1997, *ARA&A*, **35**, 1
- Davidson, K., & Humphreys, R. M. 2012, *Eta Carinae and the Supernova Impostors* (Berlin: Springer), 384
- Davidson, K., Smith, N., Gull, T. R., Ishibashi, K., & Hillier, D. J. 2001, *AJ*, **121**, 1569
- Foreman-Mackey, D., Conley, A., Meierjürgen Farr, W., et al. 2013a, *emcee: The MCMC Hammer* (USA: IOP Science)
- Foreman-Mackey, D., Hogg, D. W., Lang, D., & Goodman, J. 2013b, *PASP*, **125**, 306
- Gravity Collaboration (Sanchez-Bermudez, J., et al.) 2018, *A&A*, **618**, A125
- Groh, J. H., Madura, T. I., Owocki, S. P., Hillier, D. J., & Weigelt, G. 2010a, *ApJ*, **716**, L223
- Groh, J. H., Nielsen, K. E., Damineli, A., et al. 2010b, *A&A*, **517**, A9
- Groh, J. H., Hillier, D. J., Madura, T. I., & Weigelt, G. 2012a, *MNRAS*, **423**, 1623
- Groh, J. H., Madura, T. I., Hillier, D. J., Kruip, C. J. H., & Weigelt, G. 2012b, *ApJ*, **759**, L2
- Gull, T. R., Nielsen, K. E., Corcoran, M. F., et al. 2009, *MNRAS*, **396**, 1308
- Gull, T. R., Madura, T. I., Groh, J. H., & Corcoran, M. F. 2011, *ApJ*, **743**, L3
- Gull, T. R., Madura, T. I., Teodoro, M., et al. 2016, *MNRAS*, **462**, 3196
- Hillier, D. J., & Miller, D. L. 1998, *ApJ*, **496**, 407
- Hillier, D. J., Davidson, K., Ishibashi, K., & Gull, T. 2001, *ApJ*, **553**, 837
- Hillier, D. J., Gull, T., Nielsen, K., et al. 2006, *ApJ*, **642**, 1098
- Hofmann, K.-H., Weigelt, G., & Schertl, D. 2014, *A&A*, **565**, A48
- Hofmann, K.-H., Bensberg, A., Schertl, D., et al. 2021, *A&A*, submitted
- Hone, E., Kraus, S., Kreplin, A., et al. 2017, *A&A*, **607**, A17
- Humphreys, R. M., Davidson, K., & Koppelman, M. 2008, *AJ*, **135**, 1249
- Ishibashi, K., Corcoran, M. F., Davidson, K., et al. 1999, *ApJ*, **524**, 983
- Kashi, A. 2019, *MNRAS*, **486**, 926
- Kervella, P. 2007, *A&A*, **464**, 1045
- Lopez, B., Lagarde, S., Jaffe, W., et al. 2014, *The Messenger*, **157**, 5
- Madura, T. I., & Groh, J. H. 2012, *ApJ*, **746**, L18
- Madura, T. I., Gull, T. R., Owocki, S. P., et al. 2012, *MNRAS*, **420**, 2064
- Madura, T. I., Gull, T. R., Okazaki, A. T., et al. 2013, *MNRAS*, **436**, 3820
- Maeder, A., & Desjacques, V. 2001, *A&A*, **372**, L9
- Matter, A., Lopez, B., Antonelli, P., et al. 2016, *SPIE Conf. Ser.*, **9907**, 99070A

- Mehner, A., Davidson, K., Ferland, G. J., & Humphreys, R. M. 2010, *ApJ*, **710**, 729
- Mehner, A., Davidson, K., Martin, J. C., et al. 2011, *ApJ*, **740**, 80
- Mehner, A., Davidson, K., Humphreys, R. M., et al. 2012, *ApJ*, **751**, 73
- Millour, F., Petrov, R. G., Vannier, M., & Kraus, S. 2008, *SPIE Conf. Ser.*, **7013**, 70131G
- Millour, F., Meilland, A., Chesneau, O., et al. 2011, *A&A*, **526**, A107
- Millour, F., Lagadec, E., Montargès, M., et al. 2020, *A&A*, submitted [arXiv:2006.15660]
- Mourard, D., Monnier, J. D., Meilland, A., et al. 2015, *A&A*, **577**, A51
- Nielsen, K. E., Corcoran, M. F., Gull, T. R., et al. 2007, *ApJ*, **660**, 669
- Ohnaka, K., Weigelt, G., Millour, F., et al. 2011, *A&A*, **529**, A163
- Ohnaka, K., Hofmann, K.-H., Schertl, D., et al. 2013, *A&A*, **555**, A24
- Okazaki, A. T., Owocki, S. P., Russell, C. M. P., & Corcoran, M. F. 2008, *MNRAS*, **388**, L39
- Owocki, S. P., Cranmer, S. R., & Gayley, K. G. 1996, *ApJ*, **472**, L115
- Owocki, S. P., Cranmer, S. R., & Gayley, K. G. 1998, *Ap&SS*, **260**, 149
- Parkin, E. R., Pittard, J. M., Corcoran, M. F., & Hamaguchi, K. 2011, *ApJ*, **726**, 105
- Petrov, R. G., Malbet, F., Weigelt, G., et al. 2007, *A&A*, **464**, 1
- Petrov, R. G., Allouche, F., Berio, P., et al. 2018, *SPIE Conf. Ser.*, **10701**, 1070109
- Petrov, R. G., Allouche, F., Matter, A., et al. 2020, *SPIE Conf. Ser.*, **11446**, 114460L
- Pittard, J. M., & Corcoran, M. F. 2002, *A&A*, **383**, 636
- Richardson, N. D., Madura, T. I., St-Jean, L., et al. 2016, *MNRAS*, **461**, 2540
- Richichi, A., Percheron, I., & Davis, J. 2009, *MNRAS*, **399**, 399
- Russell, C. M. P., Corcoran, M. F., Hamaguchi, K., et al. 2016, *MNRAS*, **458**, 2275
- Schmitt, H. R., Pauls, T. A., Tycner, C., et al. 2009, *ApJ*, **691**, 984
- Schöller, M. 2007, *New Astron. Rev.*, **51**, 628
- Smith, N. 2004, *MNRAS*, **351**, L15
- Smith, N. 2006, *ApJ*, **644**, 1151
- Smith, N. 2010, *MNRAS*, **402**, 145
- Smith, N., Davidson, K., Gull, T. R., Ishibashi, K., & Hillier, D. J. 2003, *ApJ*, **586**, 432
- Soker, N. 2007, *ApJ*, **661**, 482
- Teodoro, M., Madura, T. I., Gull, T. R., Corcoran, M. F., & Hamaguchi, K. 2013, *ApJ*, **773**, L16
- Teodoro, M., Damineli, A., Heathcote, B., et al. 2016, *ApJ*, **819**, 131
- van Boekel, R., Kervella, P., Schöller, M., et al. 2003, *A&A*, **410**, L37
- Verner, E., Bruhweiler, F., & Gull, T. 2005, *ApJ*, **624**, 973
- Weigelt, G., Kraus, S., Driebe, T., et al. 2007, *A&A*, **464**, 87
- Weigelt, G., Hofmann, K.-H., Schertl, D., et al. 2016, *A&A*, **594**, A106
- <sup>6</sup> Institute for Astrophysics and Computational Sciences, The Catholic University of America, 620 Michigan Ave., N.E. Washington, DC 20064, USA
- <sup>7</sup> Department of Physics and Astronomy, San José State University, One Washington Square, San Jose, CA 95192-0106, USA
- <sup>8</sup> Astrophysics Science Division, NASA/GSFC, Greenbelt, MD 20771, USA
- <sup>9</sup> CRESST II and X-ray Astrophysics Laboratory, NASA/GSFC, Greenbelt, MD 20771, USA
- <sup>10</sup> Universidade de São Paulo, Instituto de Astronomia, Geofísica e Ciências Atmosféricas, Rua do Matão 1226, Cidade Universitária São Paulo-SP, 05508-090, Brazil
- <sup>11</sup> Département de physique and Centre de Recherche en Astrophysique du Québec (CRAQ), Université de Montréal, CP 6128 Succ. A., Centre-Ville, Montréal, Québec H3C 3J7, Canada
- <sup>12</sup> California Institute of Technology, IPAC, M/C 100-22, Pasadena, CA 91125, USA
- <sup>13</sup> Department of Physics and Astronomy, Embry-Riddle Aeronautical University, 3700 Willow Creek Rd, Prescott, AZ, 86301, USA
- <sup>14</sup> European Southern Observatory, Casilla 19001, Santiago 19, Chile
- <sup>15</sup> European Southern Observatory, Karl Schwarzschild Strasse 2, 85748 Garching, Germany
- <sup>16</sup> Instituto de Astronomía, Universidad Nacional Autónoma de México, Apdo. Postal 70264, Ciudad de México 04510, Mexico
- <sup>17</sup> Departamento de Ciencias Físicas, Facultad de Ciencias Exactas, Universidad Andrés Bello, Fernández Concha 700, Las Condes, Santiago, Chile
- <sup>18</sup> School of Physics, Astrophysics Group, University of Exeter, Stocker Road, Exeter EX4 4QL, UK
- <sup>19</sup> Department of Materials Science and Applied Mathematics, Malmö University, 20506 Malmö, Sweden
- <sup>20</sup> Department of Physics, University of Maryland, Baltimore County, 1000 Hilltop Circle, Baltimore, MD 21250, USA
- <sup>21</sup> School of Physics and Astronomy, University of Birmingham, Edgbaston, Birmingham, B15 2TT, UK
- <sup>22</sup> University of Kiel, Institute of Theoretical Physics and Astrophysics, Leibnizstrasse 15, 24118 Kiel, Germany
- <sup>23</sup> Anton Pannekoek Institute for Astronomy, University of Amsterdam, Science Park 904, 1090 GE Amsterdam, The Netherlands
- <sup>24</sup> Univ. Grenoble Alpes, CNRS, IPAG, 38000, Grenoble, France
- <sup>25</sup> AIM, CEA, CNRS, Université Paris-Saclay, Université Paris Diderot, Sorbonne Paris Cité, 91191 Gif-sur-Yvette, France
- <sup>26</sup> Institute for Mathematics, Astrophysics and Particle Physics, Radboud University, PO Box 9010, MC 62 6500 GL Nijmegen, The Netherlands
- <sup>27</sup> SRON Netherlands Institute for Space Research, Sorbonnelaan 2, 3584 CA Utrecht, The Netherlands
- <sup>28</sup> Department of Astrophysics, University of Vienna, Türkenschanzstrasse 17, 1180 Vienna, Austria
- <sup>29</sup> Trinity College Dublin, The University of Dublin, Dublin, Ireland
- <sup>30</sup> Konkoly Observatory, Research Centre for Astronomy and Earth Sciences, Konkoly Thege Miklósút 15-17, 1121 Budapest, Hungary
- <sup>31</sup> I. Physikalisches Institut, Universität zu Köln, Zùlpicher Str. 77, 50937 Köln, Germany

<sup>1</sup> Max Planck Institute for Radio Astronomy, Auf dem Hügel 69, 53121 Bonn, Germany  
e-mail: weigelt@mpifr-bonn.mpg.de

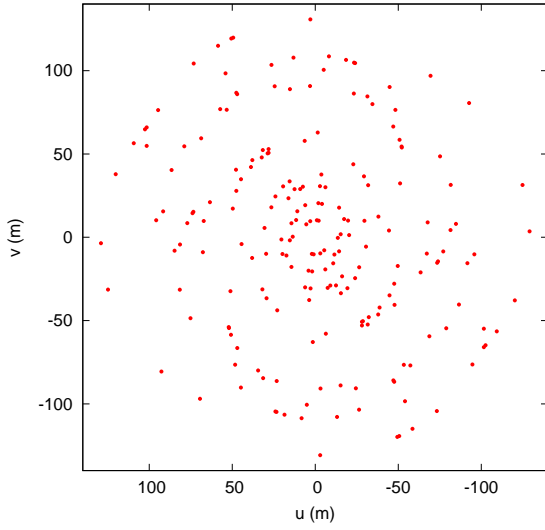
<sup>2</sup> Laboratoire Lagrange, Université Côte d'Azur, Observatoire de la Côte d'Azur, CNRS, Boulevard de l'Observatoire, CS 34229, 06304 Nice Cedex 4, France

<sup>3</sup> Leiden Observatory, Leiden University, Niels Bohrweg 2, 2333 CA Leiden, The Netherlands

<sup>4</sup> Max Planck Institute for Astronomy, Königstuhl 17, 69117 Heidelberg, Germany

<sup>5</sup> Department of Physics and Astronomy & Pittsburgh Particle Physics, Astrophysics, and Cosmology Center (PITT PACC), University of Pittsburgh, 3941 O'Hara Street, Pittsburgh, PA 15260, USA



Appendix A: Observing log and  $uv$  coverageFig. A.1.  $uv$  coverage of the observations.Table A.1. Summary of all obtained VLTI-MATISSE  $\eta$  Car data sets.

Date	Template UT <sup>(a)</sup>	Seeing target <sup>(b)</sup>	tau0 target <sup>(c)</sup>	Calibrator <sup>(d)</sup>	Seeing calibrator <sup>(e)</sup>	tau0 calibrator <sup>(f)</sup>	AT configuration
2020-02-15	01:13:49	0.47	7.68	$\lambda$ Vel	0.54	7.83	Compact
2020-02-16	01:48:56	0.35	8.25	$\lambda$ Vel	0.52	8.76	Compact
2020-02-16	04:12:13	0.99	7.31	$\lambda$ Vel	0.49	9.45	Compact
2020-02-16	06:05:59	0.40	11.30	$\lambda$ Vel	0.49	9.45	Compact
2020-02-21	02:34:18	0.69	4.90	q Car	1.53	2.74	Medium
2020-02-21	06:28:58	0.79	5.26	q Car	0.69	5.07	Medium
2020-02-21	07:43:10	0.85	3.89	q Car	0.69	5.07	Medium
2020-02-22	00:51:44	0.49	11.08	q Car	0.87	5.15	Medium
2020-02-22	03:48:01	0.79	5.39	q Car	0.68	6.18	Medium
2020-02-22	04:32:21	0.71	4.89	q Car	0.68	6.18	Medium
2020-02-22	05:45:29	1.29	3.80	q Car	1.07	4.42	Medium
2020-02-27	02:21:05	0.57	6.41	q Car	0.58	6.01	Large
2020-02-27	02:45:15	0.80	6.02	q Car	0.58	6.01	Large
2020-02-27	03:26:41	0.54	7.88	q Car	0.58	6.01	Large
2020-02-28	00:27:35	1.32	4.20	q Car	0.90	5.56	Large
2020-02-28	05:48:25	1.02	5.50	q Car.	0.83	7.18	large
2020-02-29	02:14:35	0.41	10.44	q Car	0.75	10.84	Large
2020-02-29	04:45:01	0.40	14.80	q Car	0.75	10.84	Large
2020-02-29	07:40:54	0.63	8.59	q Car	0.60	8.08	Large
2020-02-29	08:32:49	0.45	7.41	q Car	0.60	8.08	Large

**Notes.** <sup>(a)</sup>UT time at the start of the data set. <sup>(b)</sup>Seeing of the target interferograms (in arcsec). <sup>(c)</sup>Coherence time tau0 in the visible of the target data (ms). <sup>(d)</sup>Calibrator stars used for the calibration of the interferometric TF. The calibrator stars are discussed in the Appendix F. <sup>(e)</sup>Seeing of the calibrator data. <sup>(f)</sup>Coherence time in the visible of the calibrator data.

Table A.2. Summary of all obtained VLTI-MATISSE  $\lambda$  Vel data sets.

Date	Template UT <sup>(a)</sup>	Seeing target <sup>(b)</sup>	tau0 target <sup>(c)</sup>	Calibrator <sup>(d)</sup>	Seeing calibrator <sup>(e)</sup>	tau0 calibrator <sup>(f)</sup>	AT configuration
2021-02-19	03:47:56	0.51	5.19	s Car	0.57	5.59	Medium
2021-02-24	03:54:17	1.10	7.18	HD 94508	1.10	7.18	Large
2021-02-24	04:10:47	1.67	4.70	HD 104646	1.91	3.83	Large

**Notes.** <sup>(a)</sup>UT time at the start of the data set. <sup>(b)</sup>Seeing of the target interferograms (in arcsec). <sup>(c)</sup>Coherence time tau0 in the visible of the target data (ms). <sup>(d)</sup>Calibrator stars used for the calibration of the interferometric TF. The calibrator stars are discussed in the Appendix F. <sup>(e)</sup>Seeing of the calibrator data. <sup>(f)</sup>Coherence time in the visible of the calibrator data.

## Appendix B: Observables

2020-02-29T04\_45\_01-03\_37\_27.average

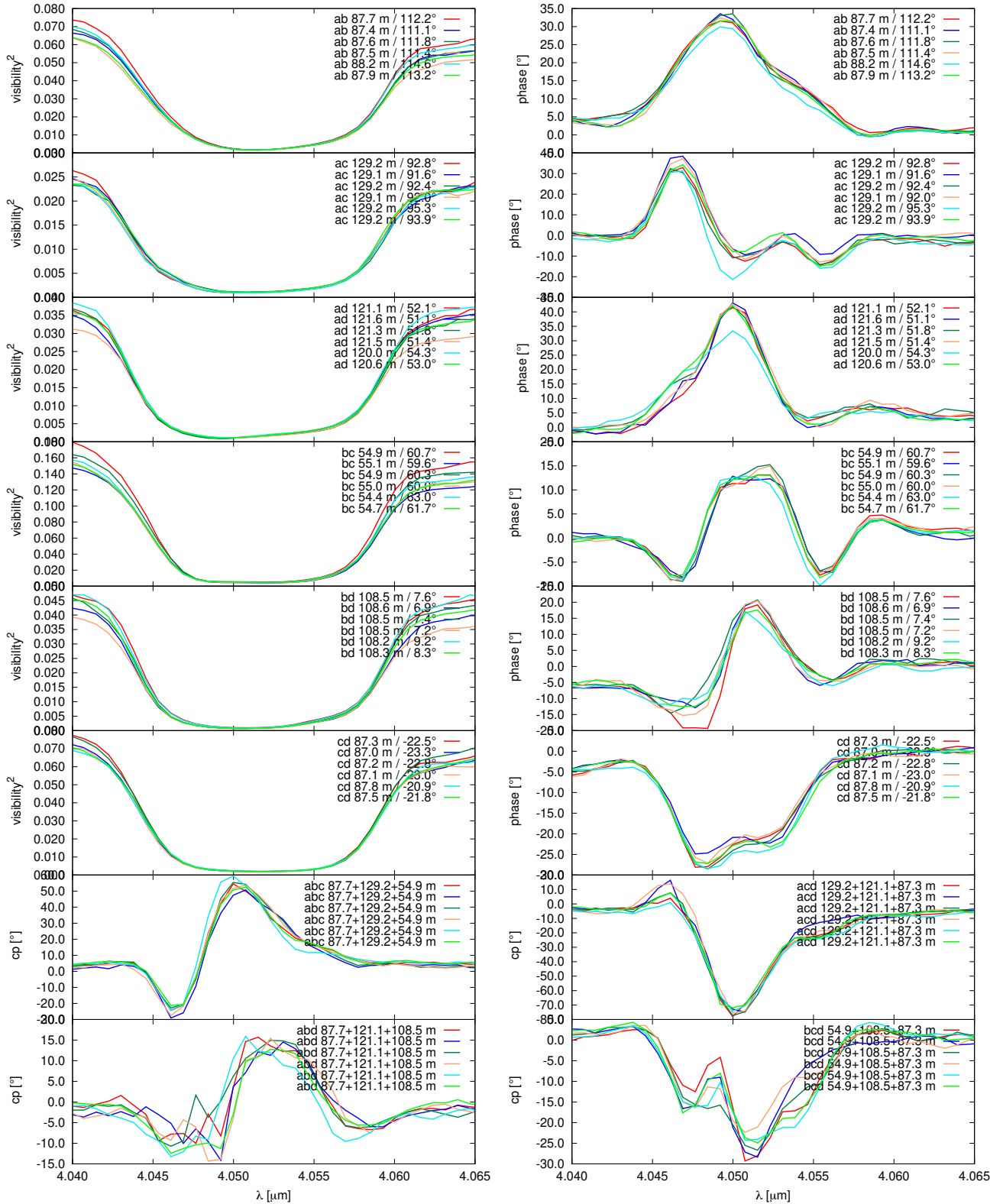
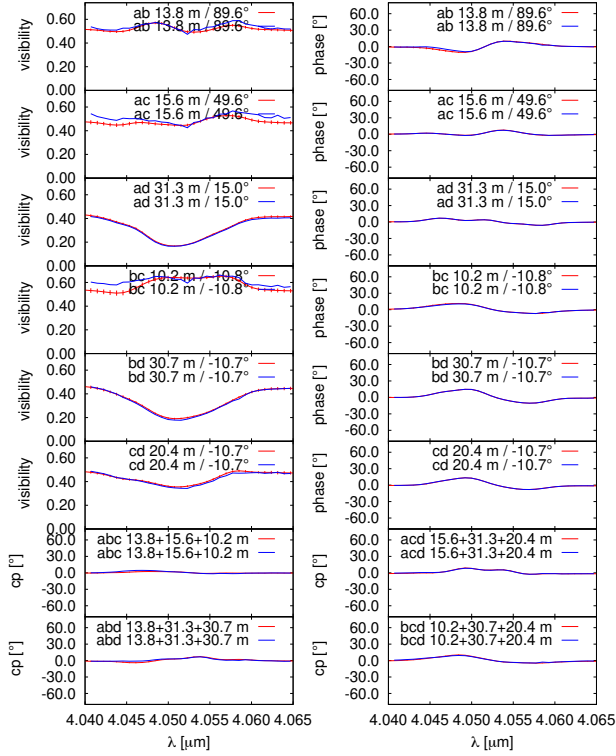


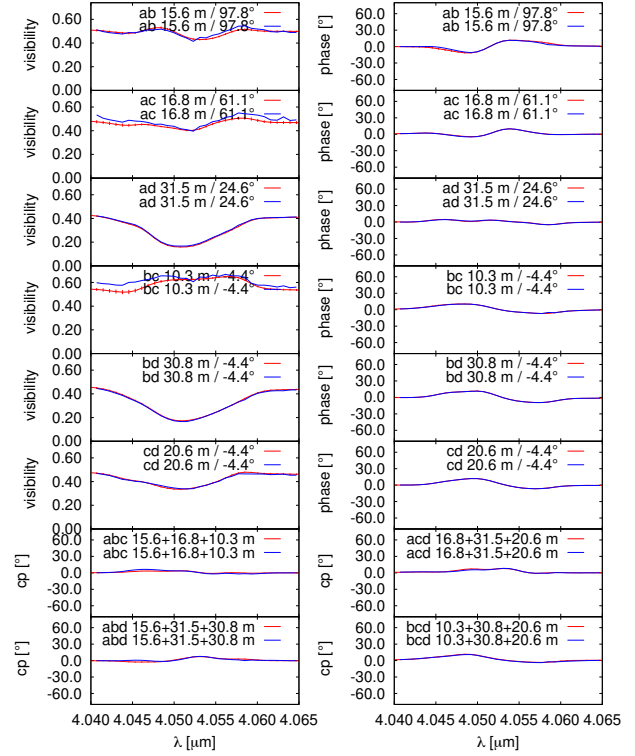
**Fig. B.1.** Illustrative example of the wavelength-dependent observables of one of the 17  $\eta$  Car measurements (projected baselines up to 129 m; see Sect. 2). The panels show the wavelength dependence of flux, visibilities, closure phases, and phases of the Fourier transform of  $\eta$  Car. Baseline lengths and PAs of the baselines are indicated in the panels. The different colored lines are measurements taken at different times (separated by  $\sim 1$  min, i.e., different atmospheric conditions) with different configurations of the MATISSE BCD.

## Appendix C: Visibilities, closure phases, and object Fourier phases derived from the reconstructed images and comparison with the corresponding measured observables

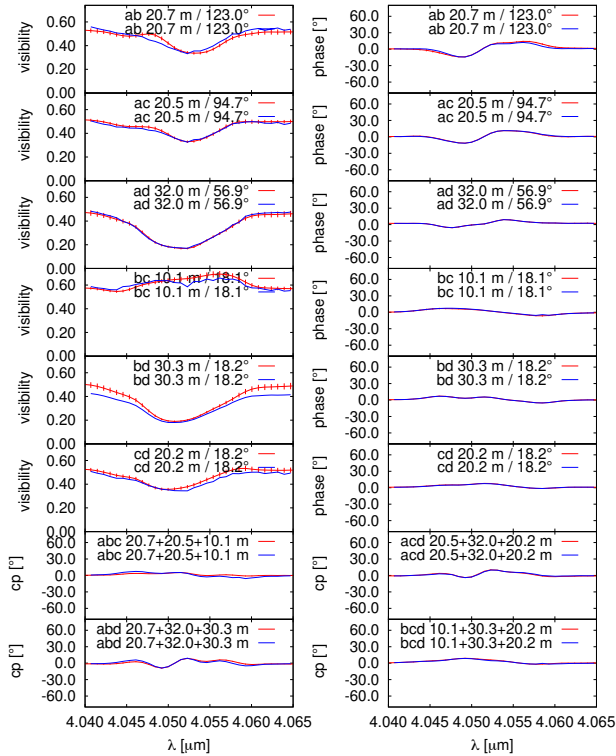
2020-02-15T01\_13\_49-00\_28\_51.average



2020-02-16T01\_48\_56-02\_36\_41.average



2020-02-16T04\_12\_13-05\_01\_26.average



2020-02-16T06\_05\_59-05\_01\_26.average

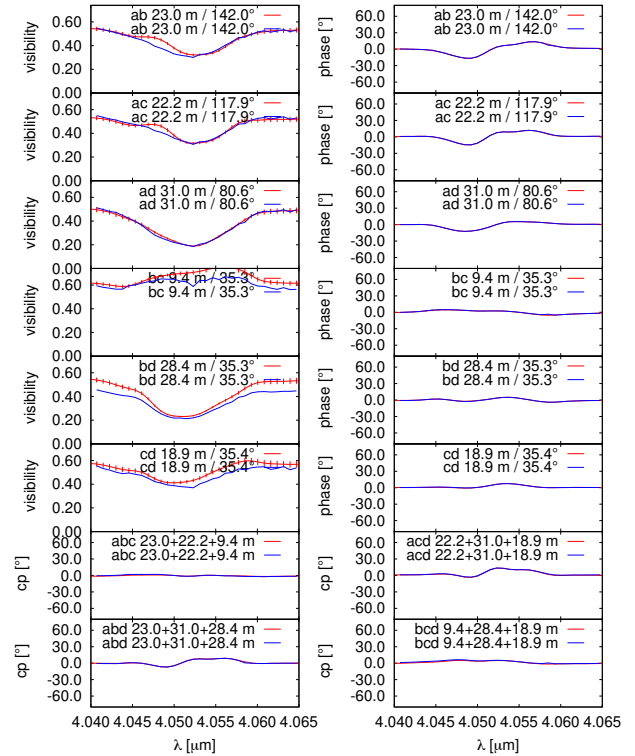
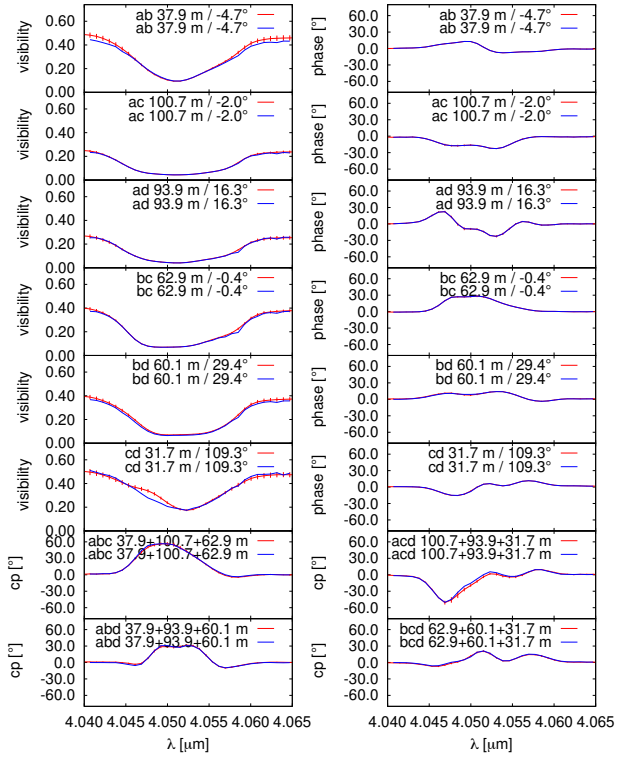
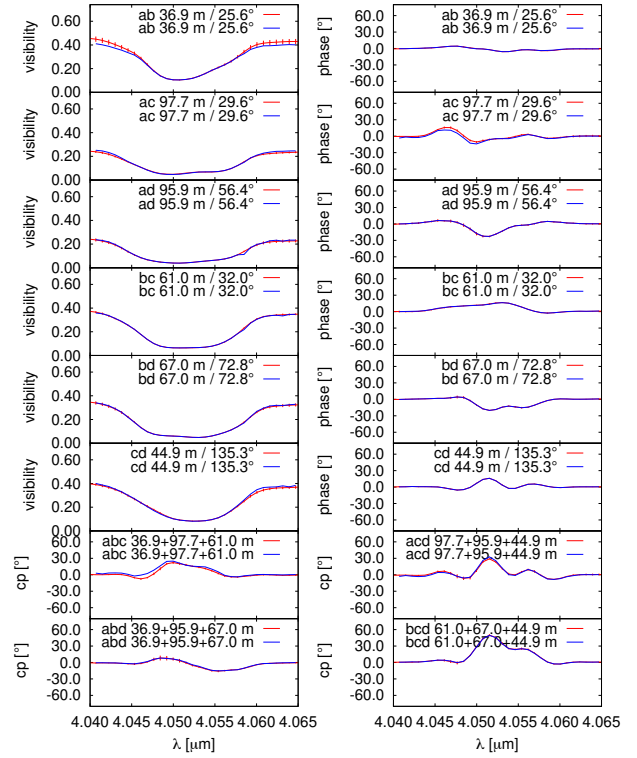


**Fig. C.1.** Comparison of the observed (red lines with error bars) visibilities, closure phases (“cp” in the figure), and phases of the object Fourier transform (“phase” in the figure) with the same interferometric quantities derived from the reconstructed images (blue lines). Dates and times of the observations are given at the top. The projected baseline lengths and PAs are inserted in each panel.

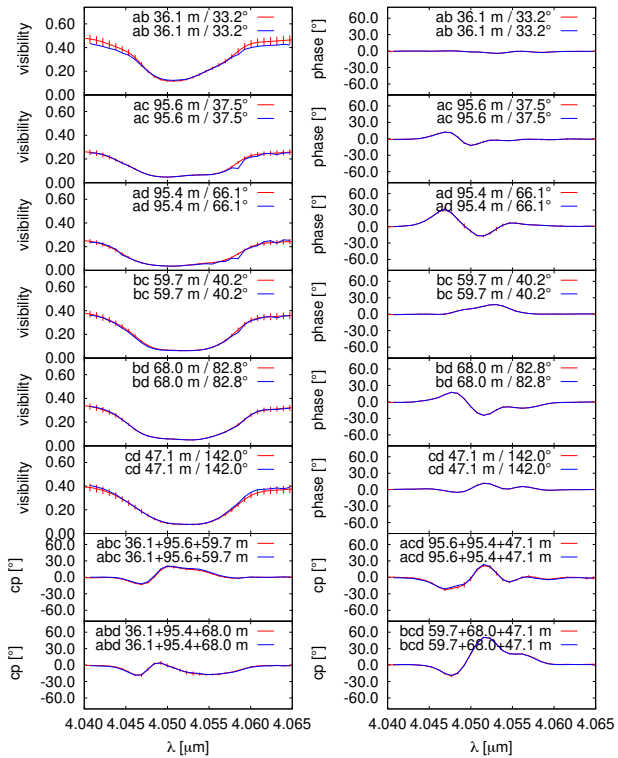
2020-02-22T00\_51\_44-01\_37\_55.average



2020-02-22T03\_48\_01-03\_21\_53.average



2020-02-22T04\_32\_21-03\_21\_53.average



2020-02-22T05\_45\_29-06\_55\_00.average

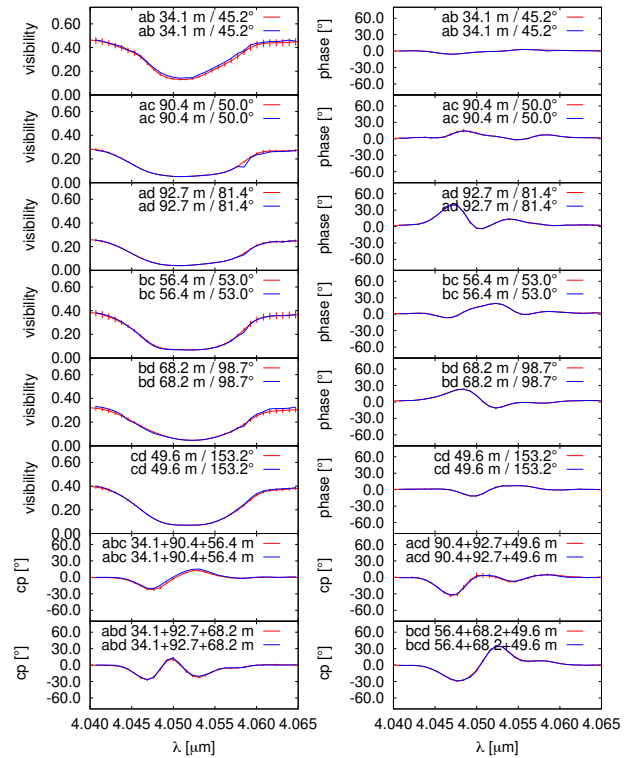
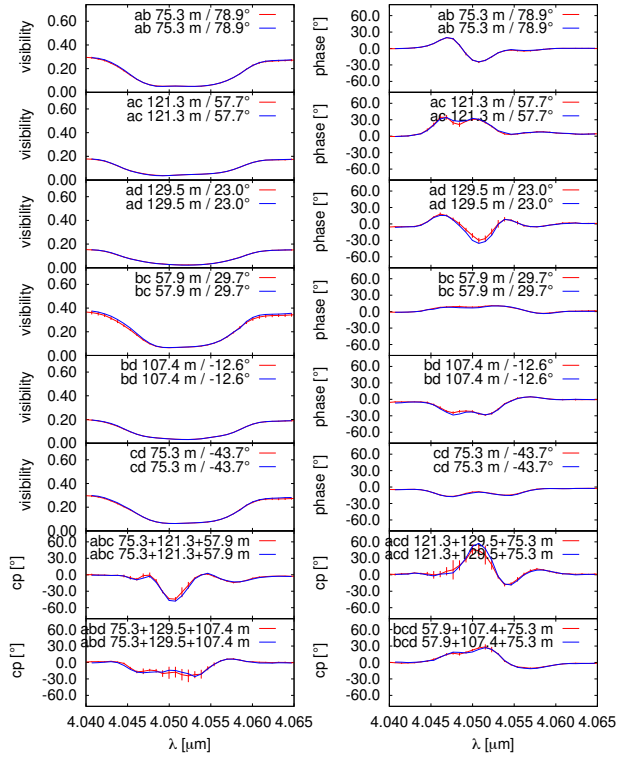


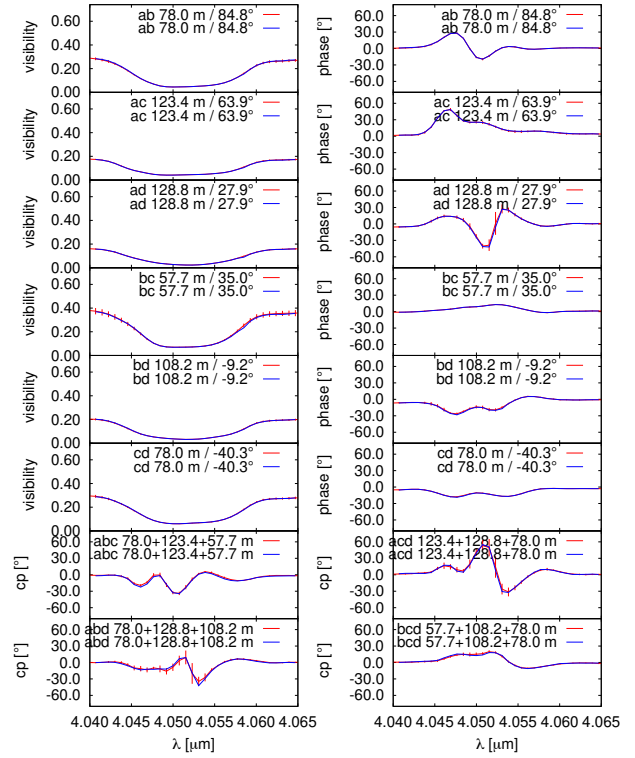
Fig. C.2. Same as Fig. C.1, but for other observations (dates and times of the observations are given at the top).



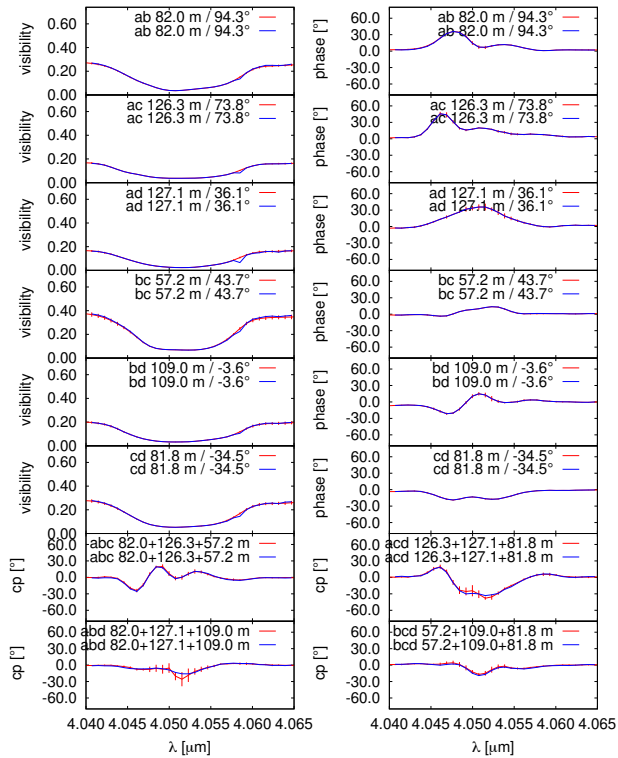
2020-02-27T02\_21\_05-03\_59\_37.average



2020-02-27T02\_45\_15-03\_59\_37.average



2020-02-27T03\_26\_41-03\_59\_37.average



2020-02-28T00\_27\_35-01\_19\_13.average

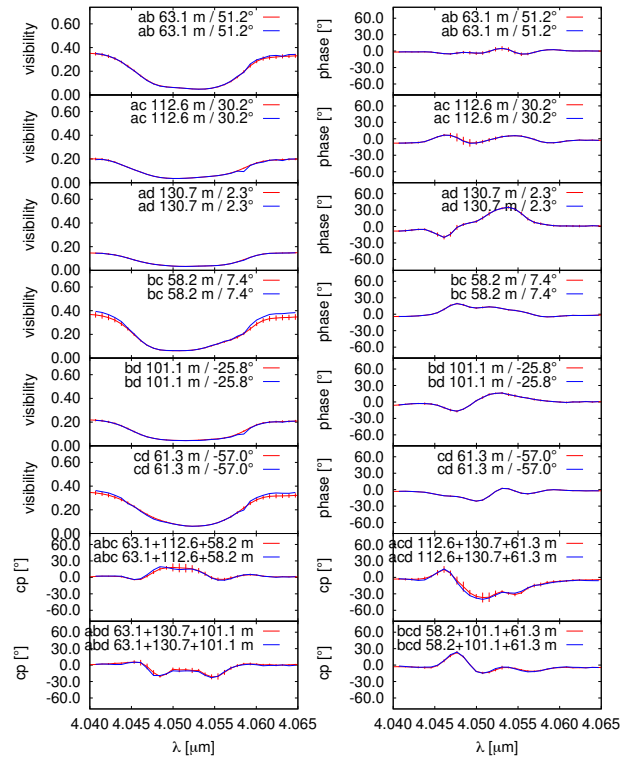
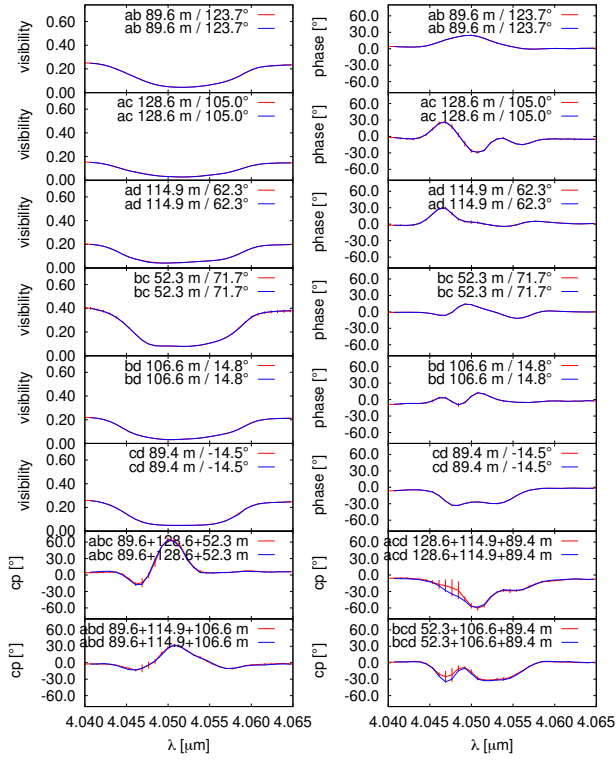
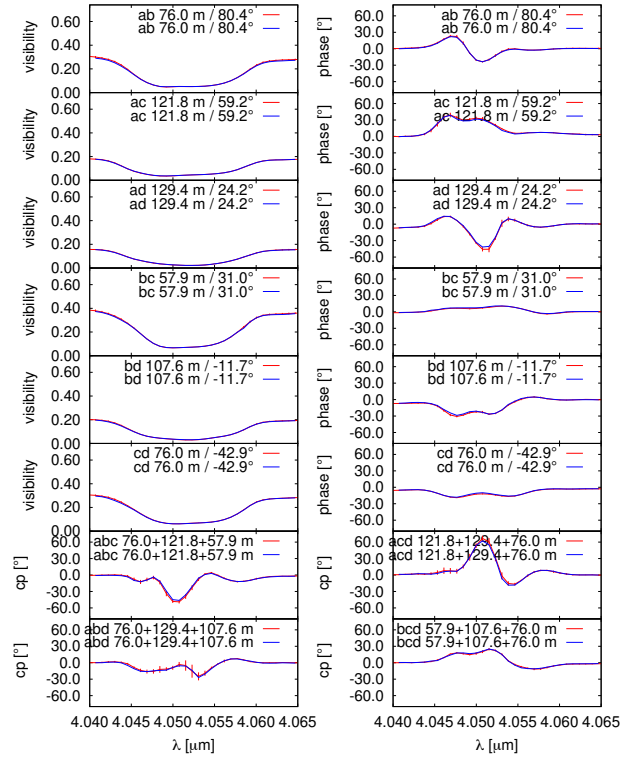


Fig. C.3. Same as Fig. C.1, but for other observations (dates and times of the observations are given at the top).

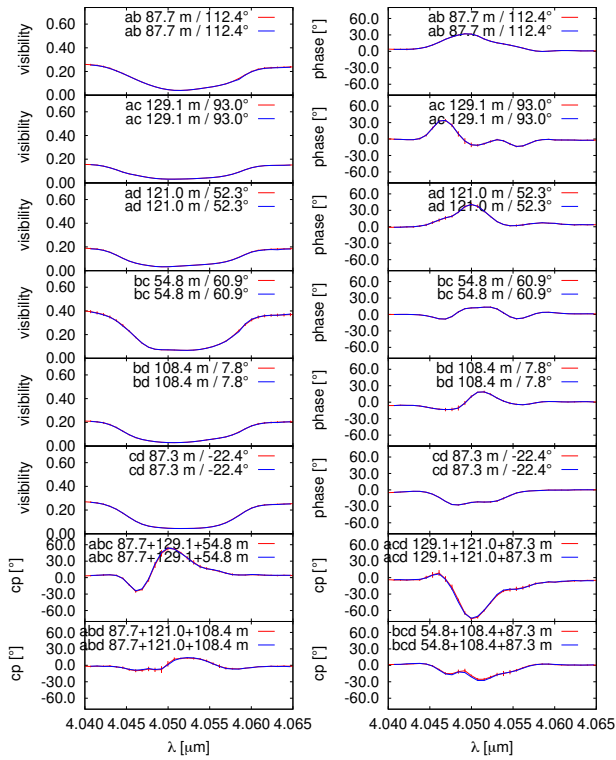
2020-02-28T05\_48\_25-05\_20\_53.average



2020-02-29T02\_14\_35-03\_37\_27.average



2020-02-29T04\_45\_01-03\_37\_27.average



2020-02-29T07\_40\_54-07\_10\_01.average

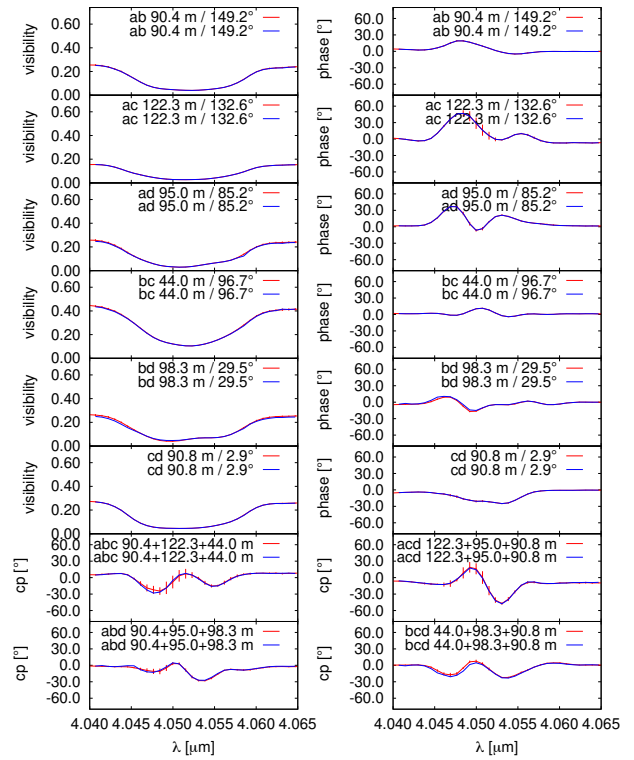
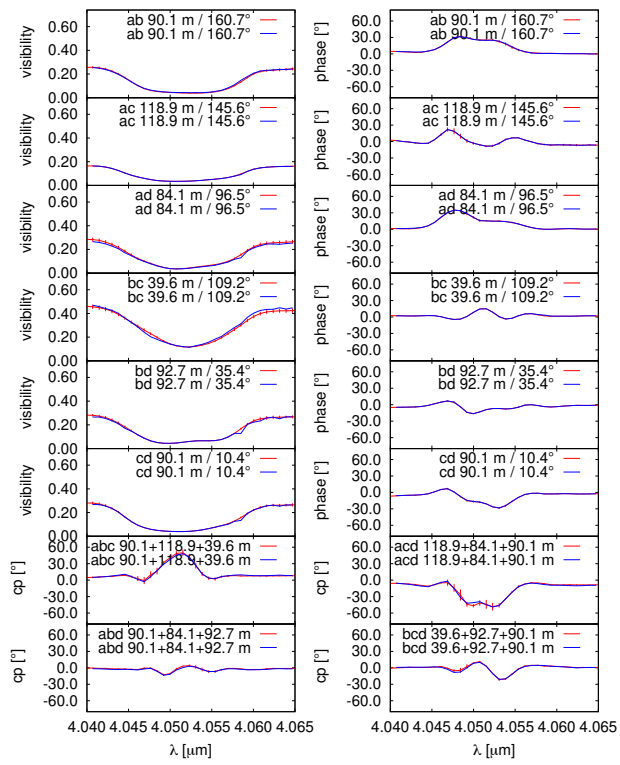


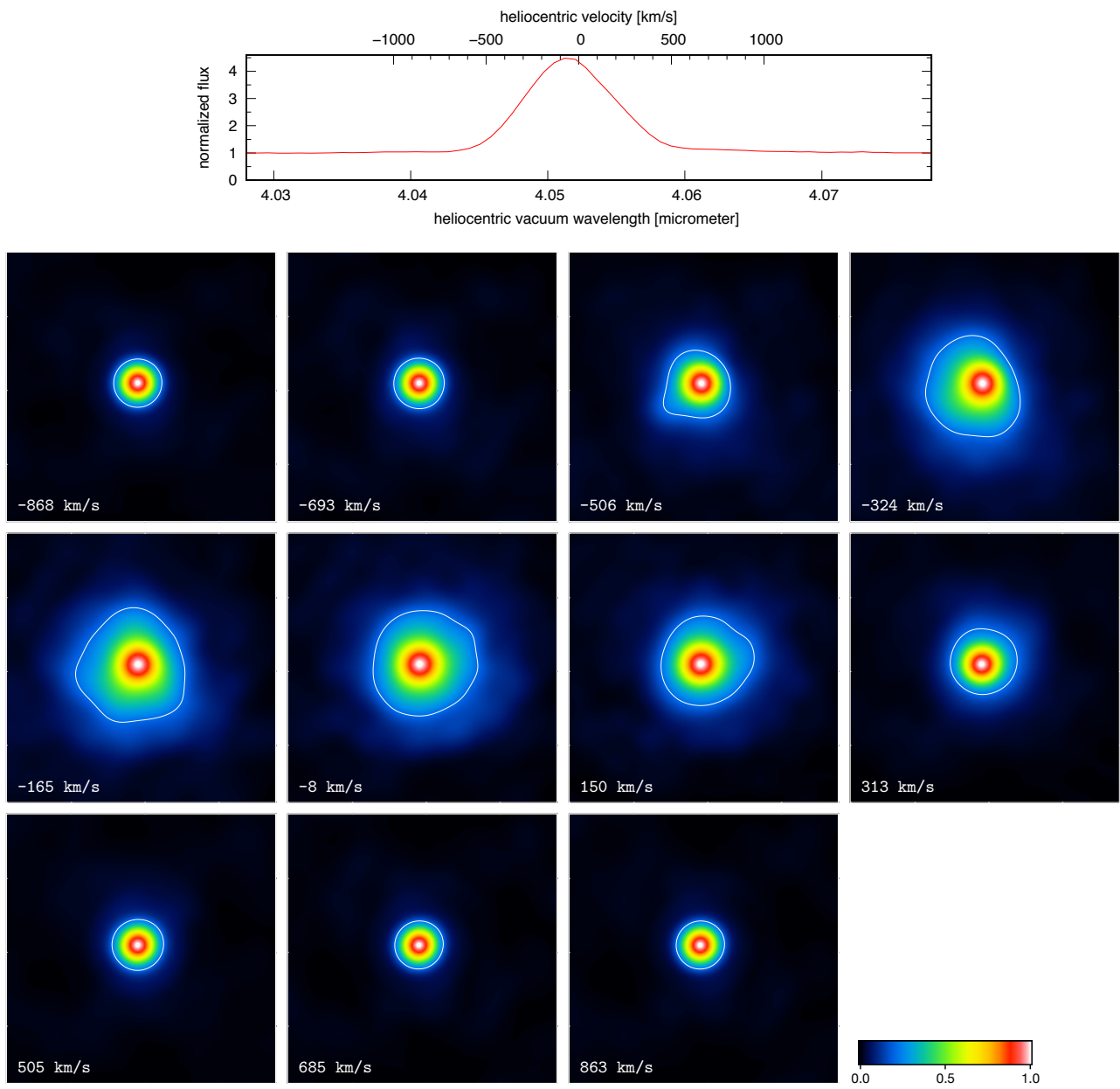
Fig. C.4. Same as Fig. C.1, but for other observations (dates and times of the observations are given at the top).

2020-02-29T08\_32\_49-07\_10\_01.average



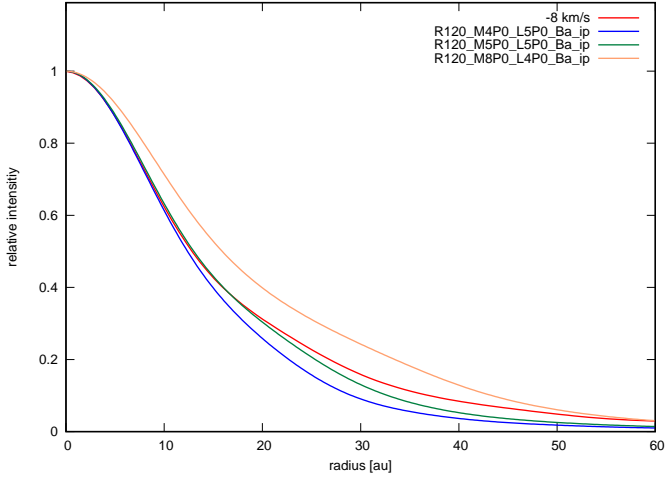
**Fig. C.5.** Same as Fig. C.1, but for other observations (dates and times of the observations are given at the top).

### Appendix D: Images of Fig. 1 normalized to unity at the brightest pixel



**Fig. D.1.** Same images as in Fig. 1, but different intensity normalization. All images are individually normalized to unity at the brightest pixel of the central peak. Contour lines are plotted at 20% and 98% of the peak intensity (the 98% contour is difficult to see but is useful for asymmetry measurements).



Appendix E: CMFGEN models of  $\eta$  Car


**Fig. E.1.** Observed  $\text{Br}\alpha$   $\eta$  Car CLV and two CMFGEN  $\text{Br}\alpha$  models with mass-loss rates of (green)  $5.0 \times 10^{-4} M_{\odot} \text{yr}^{-1}$  and (blue)  $4.0 \times 10^{-4} M_{\odot} \text{yr}^{-1}$  (all CLVs are computed for a radial velocity  $= -8 \text{ km s}^{-1}$  and spatial resolution of 6 mas). *Red CLV*: Observed CLV. *Green CLV*: Mass-loss rate  $= 5.0 \times 10^{-4} M_{\odot} \text{yr}^{-1}$ ; effective temperature  $T_{\text{eff}(\tau=2/3)} = 11\,000 \text{ K}$ ; velocity  $V_{\tau=2/3} = 326 \text{ km s}^{-1}$ . *Blue CLV*: Mass-loss rate  $= 4.0 \times 10^{-4} M_{\odot} \text{yr}^{-1}$ , effective temperature  $T_{\text{eff}(\tau=2/3)} = 12\,000 \text{ K}$ ; velocity  $V_{\tau=2/3} = 314 \text{ km s}^{-1}$ . The following parameters are identical in both models: luminosity  $= 5.0 \times 10^6 L_{\odot}$ , radius  $R_{\text{core}} = 120 R_{\odot}$ , terminal velocity  $V_{\text{inf}} = 400 \text{ km s}^{-1}$ . *Orange CLV*: CMFGEN model discussed in Sect. 5 (mass-loss rate  $\dot{M} = 8.0 \times 10^{-4} M_{\odot} \text{yr}^{-1}$ ). All models have a radius  $R_{\text{core}} = 120 R_{\odot}$  and a volume filling factor of 0.1.

## Appendix F: Diameter errors of the calibrator stars and fit error of the diameter of the continuum stellar wind

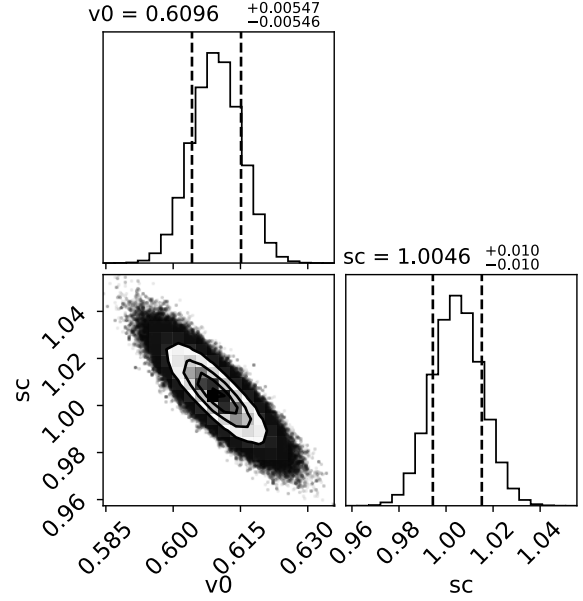


**Fig. F.1.** Posterior distribution of the fit parameters: rescaling factor (“sc” in the figure) and visibility at spatial frequency  $= 0$  (“v0” in the figure) of the 1D  $\eta$  Car CMFGEN continuum visibility fit (Fig. 8 top, red line) from our MCMC sampling. The errors are  $1\sigma$  errors.

To calculate the interferometric TF of the observations with the medium and large AT telescope configurations, we used the calibrator star q Car. Richichi et al. (2009) measured q Car  $K$ -band uniform disk (UD) diameters of  $5.245 \pm 0.046$  and  $5.270 \pm 0.024$  mas (i.e., relative errors of about 1.0% and 0.5%). The average of these two measured  $K$ -band diameters is 5.258 mas, which corresponds to the  $L$ -band diameter of 5.307 mas, if we use the wavelength dependence reported in the JSDC catalog (JMMC Stellar Diameters Catalogue - JSDC, Version 2; Bourges et al. 2017). We adopt this average  $L$ -band diameter of 5.307 mas and the above diameter error of  $\pm 1\%$  for the error estimation of the  $\eta$  Car continuum diameter discussed below.

To calculate the interferometric TF of the observations with the compact AT configuration, we used the calibrator star  $\lambda$  Vel. To measure the  $\lambda$  Vel diameter, we performed MATISSE observations of  $\lambda$  Vel together with three different calibrator stars with diameters of  $\sim 1.0$  mas (see Table A.1). The calibrators are s Car ( $1.03 \pm 0.11$  mas), HD94508 ( $1.13 \pm 0.11$  mas), and HD104646 ( $1.05 \pm 0.11$  mas) from the Mid-infrared stellar Diameters and Fluxes compilation Catalogue (MDF) (Cruzalèbes et al. 2019). Figure F.2 shows our obtained  $L$ -band visibilities of  $\lambda$  Vel. To derive the  $\lambda$  Vel diameter and take into account the uncertainties of the calibrator diameters, we created new  $\lambda$  Vel visibility data sets by varying the diameters of the calibrators by  $\pm 10\%$ , and fit UD models to these visibility data sets (MCMC fits). We obtained an average UD  $L$ -band  $\lambda$  Vel diameter of  $11.41 \pm 0.021$  mas ( $\pm 0.20\%$ ). The  $\lambda$  Vel visibilities and MCMC fit are shown in Fig. F.2.

These two above uncertainties of the q Car and  $\lambda$  Vel diameters reduce the accuracy of the diameter measurements of  $\eta$  Car’s continuum stellar wind discussed in Sect. 6. In the visibility fit of Fig. 8 (top), the above diameter errors of the calibrator stars

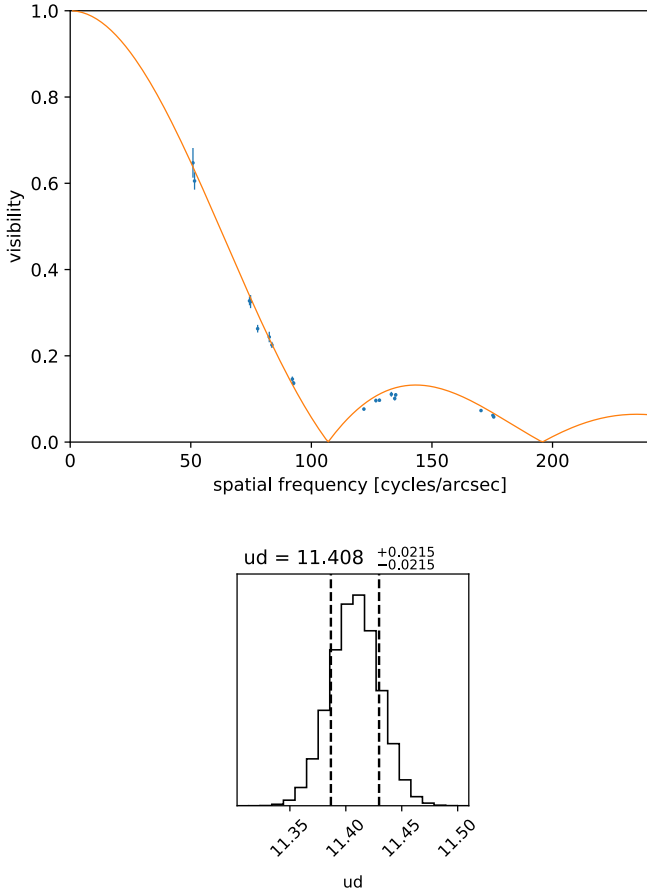


**Fig. F.2.** Diameter determination of  $\lambda$  Vel. (Top) L-band visibilities of  $\lambda$  Vel with UD fit function. (Bottom) MCMC fit of the UD diameter in mas ( $11.408 \pm 0.02$  mas;  $1\sigma$  error).

were not yet taken into account for the calculation of the wind FWHM continuum diameter. The required total error of the measured CMFGEN fit continuum diameter including the errors of the calibrator stars is estimated in the following way.

We performed four different  $\eta$  Car CMFGEN fits similar as the fit shown in Fig. 8 (top), but using four different  $\eta$  Car visibility data sets generated from the same observations of  $\eta$  Car with the following four assumptions for the calibrator star diameters: (1) the  $\lambda$  Vel and q Car diameters are 0.20% and 1%, respectively, smaller than the above calibrator diameters (i.e., q Car: 5.307 mas;  $\lambda$  Vel: 11.41 mas), (2) the  $\lambda$  Vel and q Car diameters are 0.20% and 1%, respectively, larger than the above calibrator diameters, (3) the  $\lambda$  Vel diameter is 0.20% larger and the q Car diameter is 1% smaller than the above diameters, and finally (4) the  $\lambda$  Vel diameter is 0.20% smaller and q Car diameter is 1% larger than the above diameters.

To compute the final error of our continuum  $\eta$  Car wind fit diameter including the above calibrator diameter errors, we fit the continuum CMFGEN model presented in Sect. 6 to each of the four above generated visibility data sets obtained with the described four calibrator diameter changes. The two fits, which provided the smallest (top) and largest (bottom) diameters (i.e., smallest and largest rescaling factors), are shown in Fig. F.3. Half of their diameter difference is the derived error, which is  $\pm 1.9\%$ . If we combine this error caused by the calibrator errors with the fit error of 1.0% reported in Sect. 6, we obtain a final total fit error of  $\pm 2.15\%$  (square root of the mean of the quadratic errors) for the CMFGEN fit diameter of 6.54 au of the primary stellar continuum wind intensity distribution (see Sect. 6).

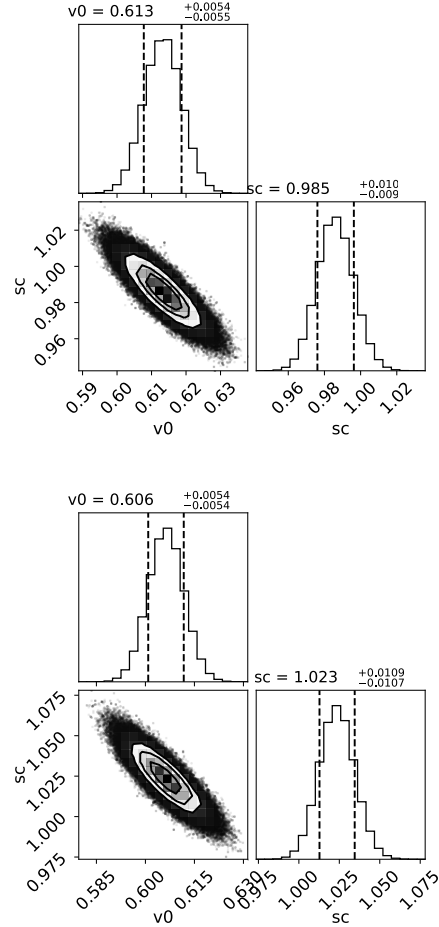


**Fig. F.3.** Two different 1D  $\eta$  Car CMFGEN continuum visibility fits. The two shown MCMC posterior distributions of the fit parameters were computed to derive the error of  $\eta$  Car's continuum diameter caused by the uncertainty of the calibrator diameters (see text). The fit parameters are the rescaling factor ("rc" in the figure) and visibility at spatial frequency = 0 (" $v_0$ ").

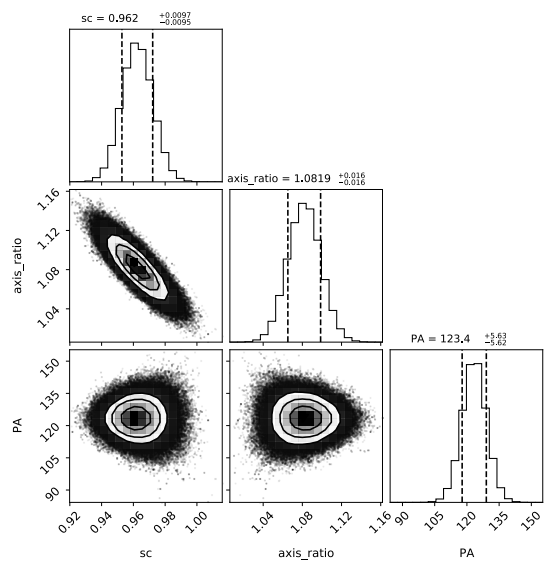


**Fig. F.4.** From top to bottom, posterior distributions of the following 2D  $\eta$  Car CMFGEN fit parameters: rescaling factor ("rc" in the figure), axis ratio of short axis to long axis (axis\_ratio), and PA of the major axis for the 2D continuum visibility fit from our MCMC sampling (errors are  $1\sigma$  errors).